



Centre Nacional de Microelectrònica. CSIC.



Universitat Autònoma de Barcelona

Thermally driven micromechanical bridge resonator

Memoria presentada por
Christian Burrer
como Trabajo de Investigación de estudios
de Tercer Ciclo en Microelectrónica

Bellaterra, Junio de 1993

Preface

Although this report has just one author, many people contributed in the course of the project and made it possible in its present form. Therefore I am especially indebted to the following persons:

Prof. Lora Tamayo, for offering me the possibility of doing a PhD at CNM.

Dr. Egelhaaf and Dr. Benz on behalf of Robert Bosch GmbH, for supporting me financially during this time.

Dr. Esteve, for his daily help, his encouragement and his supervision of this work.

Dr. Lärmer, also for his supervision, for his advice and his excellent knowledge in the subject.

Prof. Bao. He deserves a special thank you. Our collaboration during nearly one year was very close and I am in debt to him for his support and much advice during this project.

Eduardo and the clean room staff, for their helpfulness at any time, and their efforts.

Selwyn, for his translation services, his open-mindness in realizing unconventional ideas and for various collegial breaks and chats.

Zenon, who had to deal with various unusual requests and despite sometimes initial complaining, he did his best (One day you'll get the aquarium!).

Enric, who etched me some nice profiles (Schwein gehabt!).

Esteve Farrés, for his advice in questions about analog circuitry.

Mr. Fabula from IMIT for his assistance during the optical measurements.

The staff of the CNM workshop, who patiently fabricated and changed some special bits and pieces that were required, and always did an excellent job.

Santi, for his help, especially at the beginning of my stay. Thanks also for the FTIR measurements at UB.

Paco Xavi and Carlos, for offering the facilities of the old clean-room.

All who helped and advised me in the course of the last 20 months, and last but not least the sensor group of CNM.

Resumen

En este trabajo se presenta el diseño, la fabricación y la caracterización de puentes resonadores obtenidos mediante la micromecanización del silicio. Estos puentes pueden ser utilizados como elementos sensitivos en sensores mecánicos (de fuerza, presión o aceleración) debido a la influencia que las tensiones mecánicas presentan sobre la frecuencia de resonancia de los mismos.

Este trabajo se ha concebido como un paso previo a la fabricación de un sensor resonante de aceleración basado en un puente resonador. Dicho sensor se está desarrollando en la actualidad en el CNM, y los resultados obtenidos del presente trabajo han influido tanto en su diseño como en el proceso de fabricación previsto.

Las dimensiones típicas de un puente, que está situado horizontalmente sobre un agujero en la oblea de silicio y sujetado por sus dos extremos, son de $700 \times 50 \times 5 \mu\text{m}$. En sus extremos contiene dos resistencias piezoresistivas implantadas y su superficie está pasivada con una capa de SiO_2 .

Estos puentes de silicio se han fabricado utilizando técnicas de micromecanización como el grabado anisótropo húmedo y el grabado seco (RIE).

La excitación de los puentes resonadores se basa en el principio electrotérmico. Cuando se aplica un voltaje a una de las dos resistencias, ésta se calienta, estableciéndose un gradiente de temperatura entre la superficie inferior y superior del puente. Este gradiente provoca un momento de torsión que da lugar a un pequeño desplazamiento vertical del centro del puente. Si la excitación se realiza periódicamente, el puente puede oscilar, entrando en resonancia en el caso de que la frecuencia de excitación coincida con la frecuencia natural del puente.

La detección de la oscilación se realiza con la segunda resistencia piezoresistiva. El efecto piezoresistivo, que el silicio exhibe, consiste en el cambio de resistencia eléctrica a consecuencia de una tensión mecánica. De esta forma, y dado que la resistencia está localizada en una posición sensible a tensiones mecánicas y alimentada con una corriente constante, la oscilación del puente se refleja en el voltaje eléctrico de salida, cuya frecuencia se corresponde con la frecuencia de oscilación.

Para la fabricación de los dispositivos se ha aplicado el método de paro electroquímico con cuatro electrodos, en combinación con un grabado anisótropo con KOH, que permite agujerear prácticamente toda la oblea de forma controlada, y obtener así finas membranas con un control exacto de grosor. A continuación, las membranas se grabaron con RIE para obtener los puentes.

Para la caracterización de estas estructuras se ha recurrido tanto a medidas eléctricas como ópticas.

Las medidas eléctricas han consistido en registrar la función de transferencia entre las resistencias de excitación y detección al aplicar un barrido de frecuencia en el voltaje de excitación. Los picos obtenidos en la función de ganancia corresponden a la situación de resonancia mecánica. Con este tipo de medidas se ha llevado a cabo un estudio general sobre la eficacia de la excitación electrotérmica y se han comparado los distintos diseños de los puentes. También se ha estudiado el efecto de la potencia de excitación sobre la frecuencia de resonancia y el efecto de la capa de pasivación.

En cuanto a las medidas ópticas, los dispositivos también se han excitado electrotérmicamente, pero en esta ocasión la vibración se evaluó con un Laser-Vibrometer. El principio de funcionamiento de este equipo se basa en el principio de interferometría. Un rayo de láser enfocado sobre el puente vibrante se refleja parcialmente y interfiere con un rayo de referencia. De la señal de interferencia obtenida puede extraerse información acerca de la velocidad y posición del puente. Con ayuda de esta técnica se ha caracterizado la velocidad, amplitud y factor de calidad de la vibración en situación de resonancia para todos los casos considerados.

Table of contents

Preface	I
Resumen	II
Table of Contents	IV
Table of Figures	VI
I Introduction	1
1.1. Micromachining and Technology	4
1.1.1. Anisotropic wet etching	4
1.1.2. Dry Etching	6
1.2. Structure of the Report	7
II Theory of Resonators	10
2.1. Working principle of a thermally driven resonator	10
2.2. Forced vibration of a mechanical mass-spring system	13
2.3. Natural frequency of a clamped-clamped beam / Rayleighs method	19
III Design	22
3.1. Mask layers	22
3.2. Mask layout	25
IV Silicon Processing	30
4.1. Process flow	30
4.2. Electrochemical Etching	33
4.2.1. Principle	33
4.2.2. Fabrication of the resonator membranes	36
4.3. Simulated / measured parameters	37
4.4. Encapsulation / Anodic Bonding	39
4.4.1. Principle	39
4.4.2. Bonding of the resonator devices	40
V Measurements	41
5.1. Electrical Measurements	42
5.1.1. Experimental Setup	42
5.1.2. Results	45

5.2.	Optical Measurements	51
5.2.1.	Experimental Setup	51
5.2.2.	Results	54
VI Conclusions	60
References	63
Appendix A:	Plot of the maskset CNM024: Device chip resonators.	A1
Appendix B:	Process Flow Chart.	A2
Appendix C:	Suprem III Simulation Input File.	A4
Appendix D:	Cross-talk and its influence on the phase lag	A5

Table of Figures

1.1	SEM photograph of fabricated silicon resonator bridges.	2
1.2	Etch profiles obtained by anisotropic etching of a (100) wafer	5
2.1	Cross-section through a beam with width b and thickness h	12
2.2	Stress distribution in an oscillating bridge.	13
2.3	Gain and phase lag of an harmonic oscillator around resonance	16
2.4	Resonance peak with the 3dB frequencies marked for calculating the Q-factor	18
2.5	Amplitude spectrum of a 700 μ m long resonator bridge	18
2.6	Graphic illustration of equation 2.24	19
3.1	Photograph of a complete device wafer containing accelerometer and resonator chips ..	23
3.2	Plot of the mask layers on the frontside of the chip (filled black pattern: aluminium). .	25
3.3	Photograph of a processed resonator chip	26
3.4	SEM photograph of a triple bridge (length 700 μ m)	28
3.5	Resonant modes and relative frequencies of a triple bridge (from [3])	29
4.1	Standard two (left side) and three electrode setup for electrochemical etching	34
4.2	The electrochemical I/V characteristics of p-type silicon in a 40% wt. KOH solution at 75°C	34
4.3	Four-electrode configuration for electrochemical etching	35
4.4	Counter Electrode Current recorded during the last 20 minutes of the etching. The current peak, indicating passivation, is clearly visible	36
4.5	Concentration profiles of a test wafer, simulated with Suprem and measured with Spreading Resistance	37
4.6	A schematic setup for electrostatic bonding of silicon to glass	39
5.1	Experimental setup for electrical operation	42
5.2	Schematic of the buffer A_{det}	43
5.3	Schematic of a resonator bridge showing the parasitic capacitances	44
5.4	Equivalent circuit of Figure 5.3	44
5.5	Gain vs. frequency. $V_{exc}=V_{AC}$	45
5.6	Gain vs. frequency. $V_{exc}=V_{DC}+V_{AC}$	45
5.7	Bode plots of a 700 μ m long bridge. $V_{ACexc}=1V$; (A) (B) (C)	46
5.8	Bode plot of a 700 μ m long triple bridge. $V_{ACexc}=1V$, $V_{DCexc}=5V$, $P=13.7mW$	47

5.9	Different positions of excitation and detection resistors	49
5.10	Resonance frequencies versus input power of above bridge designs.	
	$V_{ACexc}=1\text{V}$, V_{DCexc} varying	49
5.11	Schematic representation of a Laser-Doppler Vibrometer	51
5.12	Schematic structure of a laser-vibrometer with frequency modulation of the reference beam	53
5.13	Experimental setup for optical readout	54
5.14	Velocity spectrum of a 700 μm long bridge	55
5.15	Velocity spectrum of a 700 μm long bridge	56
5.16	Velocity spectrum of a 700 μm long triple bridge	56
5.17	Velocity spectrum of a 700 μm long triple bridge	57
5.18	Velocity spectrum of a 500 μm long single bridge	57
5.19	Velocity spectrum of a 500 μm long triple bridge	57
D.1	Resonance circle of a mechanical harmonic oscillator	A-5
D.2	Resonance circle of an oscillator with constant cross-talk	A-5
D.3	Vectorial addition of mechanical resonance and cross-talk	A-6
D.4	Transfer function of a resonator bridge	A-6
D.5	Equivalent circuit representing the cross-talk (see section 5.1.1)	A-7
D.6	Resonance circle of a resonator bridge	A-7

I Introduction

Since silicon micromachining has become a key technology for the fabrication of sensors, current research focuses, amongst other things, on the development of high-precision measurement devices. Exacting standards are required for military and aerospace applications, but also in the automotive field, where primarily sensors for measuring accelerations and pressure find their application.

One sensor type that intrinsically offers a high measurement resolution and that has been known for a long time, but up until now can rarely be found among commercial products, is the resonant sensor. The approach is to use variable stress in a mechanical structure to change its frequency of vibrational resonance, for example by changing the tension in a stretched string [1]. Advantages of a resonant sensor are its high stability - we think of a simple quartz wrist watch, whose resonating mechanical quartz element is extremely frequency stable and does not have to be corrected for years - a very high resolution, and the quasi-digital frequency output. A frequency output is highly compatible with digital circuitry and less noise sensitive than, for example, voltage outputs. If the sensor is also made from silicon, another benefit arises, both the mechanical sensor and the electrical conditioning circuit can be fabricated on the same chip, moving towards the smart sensor.

A number of sensor prototypes based on the resonant principle have been fabricated so far, we shall just mention some examples. Satchell and Greenwood were the first who presented a resonant silicon accelerometer [2]. Their prototype consisted of a slim silicon beam and two flexure hinges, supported by a seismic mass. The beam had diffused piezoresistors and was excited electrothermally into resonance. Sensing was performed with the second stress-sensitive piezoresistive resistor. An acceleration stretched or compressed the beam, leading to a change of its resonance frequency. By conditioning the sensed signal and feeding it to the excitation resistor, the sensor operated as a closed mechanical oscillation circuit. A similar approach was demonstrated by Chang and Putty, but in contrast they were using electrostatically driven and sensed polysilicon beams [3].

Among resonant pressure sensors, the design of Petersen et al. stands out. It consists of a thin silicon beam on a silicon membrane, made by silicon-silicon bonding and an etch-back technique [4]. The beam is driven and sensed piezoelectrically and operates in vacuum. Reported qualities and performances of this sensor are impressive, emphasizing the potential of the resonant principle for sensors.

Although the actual report does not deal directly with resonant accelerometers, it is closely related to the subject. We present a study and evaluation of micromachined resonant silicon bridges, which will be the vibrating element of a future resonant accelerometer. This sensor is being developed at CNM. Its concept has already been worked out and it will soon be fabricated.

The excitation principle that was chosen for the bridges, some fabricated devices can be seen in

Figure 1.1, is based on electrothermal driving [5,6].

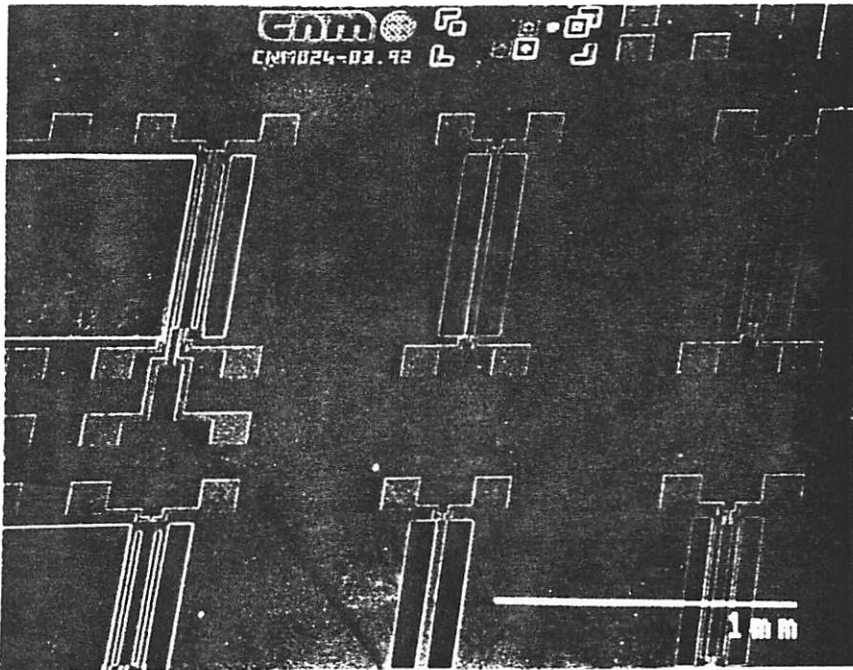


Fig. 1.1: SEM photograph of fabricated silicon resonator bridges.

Excitation via a periodic heating force is very popular, since it requires only a power-dissipating resistance on the vibrating element - usually a diffused or implanted silicon resistor or a deposited polysilicon resistor are utilized - and a periodic driving voltage or current.

On the other hand the mechanical characteristics of silicon are very temperature sensitive and the heating can enhance undesired drift effects.

For sensing the bridge motion we selected the piezoresistive detection principle, based on the piezoresistive effect of silicon. Both electrothermal excitation and piezoresistive detection were also chosen with respect to the future operation of the bridges in an acceleration sensor. The oscillation will be maintained in a closed circuit by processing the detection signal and feeding it into the excitation resistor.

Before proceeding to the organization of the report, we will present a short survey of the micromachined resonator in literature. In 1968 Wilfinger et al. first proved that a silicon structure with diffused resistors - in their case a cantilever beam - could be brought into resonance by periodic heating and detected piezoresistively [7]. The beam was sawn from a silicon wafer and had rather macroscopic sizes, 5mm length, 0.5mm width and 130 μ m thickness. In the following years, several papers on micromachined cantilever beam resonators were published [8,9]. Othman, e.g., demonstrated that beams with resonance frequencies up to 500kHz (!) could be driven electrothermally [8]. Whereas these resonators were all made from silicon, some examples using other

materials originating from the IC field must be mentioned. Bouwstra et al. presented an electrothermally driven resonant mass flow sensor, whose resonating bridge consisted of silicon nitride and contained two embedded polysilicon resistors [10]. In view of the sensing principle of their device, based on the cooling effect of a gas passing over the resonator, they had to choose the opposite approach and make the oscillating element very temperature sensitive. Therefore, and for process-related reasons, they selected two materials with very different thermal expansion coefficients. For the silicon bridges presented here or any other resonator used in a temperature stable sensor, the temperature sensitivity of the oscillating elements must be kept as low as possible.

Recently, thermally driven resonator bridges made of silicon oxide with an aluminium mirror on top were reported [11]. The mirror served for optical measurements, and readout of the oscillation was performed acoustically and piezoresistively.

The silicon resonator bridges were designed, fabricated and characterized at CNM in collaboration with Robert Bosch GmbH, Stuttgart. Part of the characterization was performed at the Institut für Mikro- und Informationstechnik in Villingen/Schwenningen. Thickness measurements of the devices were carried out at the University of Barcelona.

In the next subsection an introduction on the micromachining technologies, that were employed for the fabrication, is given. Subsection 1.2. describes the structure of the report.

1.1. Micromachining and Technology

In general terms micromachining is the forming of three-dimensional mechanical microstructures. The materials used originate from the field of IC-technology like silicon, gallium arsenide or quartz. In the past few years polysilicon [12] has also become more and more popular. Silicon, especially, has excellent properties like high stiffness together with high elasticity [13].

Physical forming of silicon is done by etching. A silicon wafer is exposed to a fluid etchant, a plasma etchant or an ion beam. The etching process can be physical or chemical.

In silicon micromechanics, there are two major fields of research: *Surface micromachining* and *bulk micromachining*. In surface micromachining, the silicon substrate is used as a foundation and alternate layers of SiO_2 and polysilicon are deposited on top; when complete, the oxide is removed and the remaining freestanding polysilicon is then used as the mechanical structure. In bulk micromachining, the silicon substrate is etched and sculpted to leave the structure.

One of the main applications in micromachining is the development and fabrication of optoelectronic devices and especially of sensors. We mainly consider mechanical sensors for measuring parameters such as pressure, acceleration, force and flow etc. A growing market for low cost and large volume sensors exists, steering sensor development towards the 'smart' sensor, which contains mechanical sensing element and signal-processing circuit on the same silicon chip.

Next we briefly describe the two main silicon bulk micromachining fabrication techniques, that were both employed for the fabrication of the resonator devices.

1.1.1. Anisotropic wet etching

Anisotropic wet etching of silicon, defined by the dependency of the etch rate on the crystal orientation, is one of the most important and well-established techniques in micromachining. Hydroxide-water solutions (such as CsOH , KOH , NaOH , NH_4OH and recently TMAH (Tetra-methyl-ammonium-hydroxide, $(\text{CH}_3)_4\text{NOH}$)) together with EDP-water solutions (Ethylenediamine-pyrocatechol, $\text{NH}_2(\text{CH}_2)_2\text{NH}_2 - \text{C}_6\text{H}_4(\text{OH})_2$) and hydrazine-water solutions ($\text{N}_2\text{H}_4 - \text{H}_2\text{O}$) are the main wet etchants. They all have in common that the etch rate of $\{111\}$ silicon planes is much smaller than that of $\{100\}$ or $\{110\}$ planes. When etching $[100]$ oriented silicon, the typical 54.7° angle to the substrate surface as shown in Figure 1.2 results. Traces of $\{111\}$ planes intersecting the (100) surface form right angles with each other.

Different explanations for this behaviour (in the case of KOH) like the higher package density of atomic bonds or the higher activation energy of binding forces of $\{111\}$ planes exist. The latter, established by Seidel et al., is the most conclusive one [14]. They attribute the lower etch rate of $\{111\}$ planes to their lower number of dangling bonds (free silicon bonds) per unit cell at the surface,

compared to {100} or {110} planes. In their model, each silicon atom at the surface of a {100} or {110} plane has two dangling bonds and two bonds to neighboured Si-atoms (backbonds), whereas in {111} planes an Si-surface atom has only one dangling bond and three backbonds. An intermediate step during the etching is the reaction of an (OH) molecule with a silicon atom. To remove an atom from the surface, therefore, in a {111} plane, three backbonds have to be 'broken' instead of only two in the case of {100} or {110} planes. By reaction with an (OH) molecule the backbonds are weakened and can be broken. According to Seidel a surface atom of a {111} plane with three backbonds is in a more stable state and a higher activation energy is necessary to break it off.

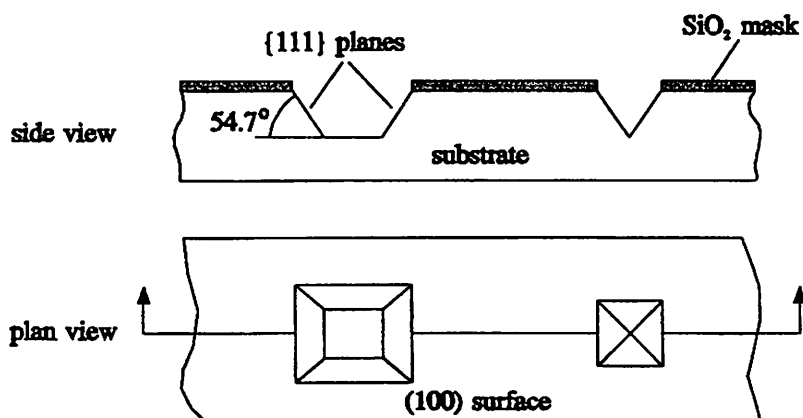


Fig. 1.2: Etch profiles obtained by anisotropic etching of a (100) wafer.

The advantage of EDP over hydroxide solutions is that it etches neither aluminium, nor silicon oxide. Thus IC-processed wafers can be etched without special passivation films in an EDP based etch solution. Nevertheless EDP is a known carcinogen, which restricts its wide application.

Among the hydroxide solutions, KOH is still the etchant most used. It has the advantages over other wet etchants that it etches fast and the process repeatability is high. KOH solutions are very stable, that means that their etch characteristics do not depend much on the amount of silicon diluted in the etch solution. Moreover the running costs are low and the solution is nontoxic. Against these advantages there are two drawbacks:

The potassium ions contained in the etch solution, which become mobile at temperatures above approximately 100° C, can diffuse into oxide films and create mobile ion charges. In the case of the gate oxide of MOS transistors, this can degrade their characteristics. Extensive cleaning in a chlorine ambient - usually a hot HCl-H₂O₂-H₂O solution (RCAII clean) is used for removing potassium ions on KOH etched wafers - minimizes the contamination risk. Nevertheless KOH solutions are banished from many clean rooms and thus wet etching is often constrained to the final step of the fabrication process. The second inconvenience of KOH is that it etches aluminium and silicon oxide, unless thermally grown oxide, at a fairly high rate. Commonly silicon nitride, either plasma or vapour deposited, is used as passivation film. Its etch rate in KOH is almost negligible.

Recently TMAH, a positive photoresist developer compound, has been found to be an anisotropic wet

etchant [15]. Due to its IC compatibility and its negligible etch rate of silicon oxide, it is a very promising candidate to substitute for KOH in certain applications in the near future. Though in some respects such as running costs, etch rate and stability of the etch solution, it cannot compete with KOH.

For the wet etch step of the fabrication of the resonator bridges, a KOH solution was used, therefore we shall list briefly some of its characteristics:

- Etch rate of <100> oriented silicon. Depends on temperature and concentration. It increases with temperature, the highest etch rates are obtained for 20-30% weight KOH diluted in H₂O. Typical value at CNM (Temperature 75°C, concentration 40% wt.) approximately 0.7µm/min. Concentrations lower than 20% wt. produce rough and hilly surfaces, for good surfaces a concentration higher than 30% is required.
- Etch rate of SiO₂ (thermally grown). Also depends upon temperature and concentration, typical etch rates are 0.1-0.5µm/h [16]. When SiO₂ is used as masking material, both temperature and concentration of the solution should be kept as low as possible.
- Etch rate of Si₃N₄. Negligible (approximately 14Å/h [17]). It is therefore a perfect masking material. Aluminium is etched while chromium and gold are not affected by KOH.
- Etch ratios for {100} to {111} oriented planes. Up to 400 are reported [18]. However, even a slight misalignment reduces this ratio to less than 100. Typical value at CNM approximately 50..100.
- Highly boron doped silicon (concentration greater than 5·10¹⁹ cm⁻³) is not etched and can be used as an etch-stop.
- The electrochemical etch-stop in KOH (see also subsection 4.2.) permits the fabrication of diaphragms and membranes with a very precise thickness control.

1.1.2. Dry etching

Generally, dry etching processes are characterized so that the material to be removed reacts with gaseous ions, and the reaction product, that is also gaseous, can then be transported away. The process takes place in a vacuum chamber, where the wafer to be etched is located on a ground electrode. In the chamber a plasma is generated from the source gas(es) by an RF generator. Because of the DC autopolarization of the ground electrode, the reactive ions in the plasma are accelerated towards the wafer. The etching mechanisms can be physical or chemical and are very often a combination of both. In plasma etching, characterized by relatively small DC voltages between electrode and plasma, the dominating removal mechanism is chemical. The plasma reacts chemically at the wafer surface with the material to be etched, forming volatile products. They are pumped away by the vacuum pump. Physical removal is a more important mechanism in Reactive Ion Etching

(RIE). High voltages between electrode and plasma accelerate ions towards the wafer, where they react chemically with the material to be etched and also sputter it away physically due to their kinetic energy.

Important process requirements in dry etching are a high degree of anisotropy (ratio of vertical etch rate to lateral etch rate), a high selectivity to substrate and etch mask, a high etch rate, a high degree of etch rate uniformity across the wafer and from wafer to wafer and a low heating of the substrate surface when working with a resist protection mask.

For bulk micromachining applications, where mainly silicon is etched, both high anisotropy and high selectivity, two conflicting parameters, are of special importance. RIE processes are generally anisotropic, but have a poor selectivity, whereas plasma processes exhibit good selectivity but are usually more isotropic.

Typical silicon etch masks are photoresist, silicon dioxide and aluminium. Aluminium offers the best masking properties, but its application is often restricted by the fabrication process. Silicon oxide films, either grown or deposited, are suitable for many applications, moreover they can be integrated easily into practically all fabrication processes.

Many source gases exist, usually chlorinated (C_2ClF_5 , Cl_2), flourinated (CF_4 , SF_6), brominated (HBr, $CBrF_3$) gases, or a combination of them are currently used [19,20].

When etching with carbon-containing source gases, under certain conditions, polymeric material can form and deposit at the sidewalls of the etch groove. This autopassivation effect is very useful for etching deep trenches with vertical sidewalls. The same effect can be achieved by using photoresist as a masking material. The removed resist is nonvolatile and can stick to and react with vertical surfaces not exposed to ion bombardment. For this reason photoresist has become very popular as an (additional) masking film for dry etching in micromachining processes.

1.2. Structure of the report

This report is divided into four parts: With regard to the topic - micromachined resonant devices - we first present a short introduction in the field of vibration and resonance. Next, the fabrication of the resonators is described. This process consists of two stages, design and fabrication. An important section is dedicated to the actual fabrication processes, where several micromachining techniques, that had been previously developed at CNM, were applied for the first time for the fabrication of a micromechanical device. Finally we describe the methods we used for the characterization of the devices. The results show that the devices, as they were conceived, work satisfactorily and can be integrated into a future resonant sensor. Thus the initial aim of this project, proving the feasibility of thermally driven micromachined bridge resonators, has been achieved.

Section 2 of the report is devoted to an introduction of the resonance phenomena. We present its mathematical description with the help of a basic model, the classic spring-mass system. This harmonic oscillator is, due to its simplicity, a model for many real systems, and can be found in any literature dealing with vibration and resonance. Our aim in this introduction is not to present an all-embracing theory, that can be found in many books, but to give the reader a feeling of the notions of vibration and resonance. In the second part of section 2 we demonstrate a technique for calculating analytically the resonance frequency of a vibrating bridge. Rayleigh's method is a well known tool and, in the case of simple mechanical structures like a straight bridge, its easy application and accuracy makes it a good alternative to numerical simulations.

In section 3 we present the design of the devices, that had been guided by two conditions: First, the thermal excitation principle and the desired resonance frequency and second, the chosen process technology. We focus on the different bridge designs, their properties are laid down and their incorporation is justified. The finally selected designs were arranged on a 5.5x5.5mm large chip. For a better understanding of the different mask levels in the mask layout, we also include here some information about specific process steps.

Section 4 covers the whole fabrication process, including initial process simulations and subsequent parameter measurements. First, the flow chart is outlined, showing the integration of the micromachining steps into the 'standard' IC-process. Although the anisotropic etching with electrochemical etch-stop at a p/n-junction is an established process at CNM, it was the first time that it had been used in a complete fabrication process. For this reason an introduction to the subject is given, followed by the results obtained.

We carried out process simulations to calculate the expected parameters, and these are compared with the parameters achieved.

The second part of section 4 deals with the preparation of the devices for the final measurements, the encapsulation. In IC technology, encapsulation is usually not a delicate process. The chips are sawn, glued onto a package and wire bonded. For micromechanical devices, however, encapsulation is one of the key process steps. Their fragility and susceptibility to mechanical stresses require special technologies. We present one of them, anodic bonding. Its principle and application to resonator devices is explained. This bonding process allows stress-free sealing of a silicon chip to a rigid glass chip.

Section 5, finally, is dedicated to the characterization of the devices. As the introduction indicated, the resonators were designed for electrothermal driving and piezoresistive detection. However motion can also be sensed with optical techniques. We performed both electrical and optical measurements. In the electrical measurements, the transfer function between the two resistors was recorded, sweeping

the excitation frequency. A peak indicated resonance. The measurements included a general study of the efficiency of thermal drive, comparisons between the different designs, the effect of the driving power on the resonance frequency and the effect of the passivation layer on the resonance frequency. The optical measurements were possible because of the courtesy of the Institut für Mikro- und Informationstechnik in Villingen/Schwenningen, that provided the necessary equipment and enabled the characterization at their site. We had at our disposal a laser-vibrometer, whose working principle is based on interferometry. A laser beam is focused onto the vibrating object and partially reflected. The reflected light interferes with a 'reference' beam, and the resulting interference signal contains information about velocity and location of the object. This signal is analyzed with a DSP. Our measurements included velocity, amplitude and quality factor of the bridge vibration at resonance. As expected, results of both measurements types agree well.

II Theory of Resonators

This section is devoted to an introduction of the theory of resonance.

First, we explain in a few words the working principle of a thermally driven silicon resonator bridge. Next the phenomena resonance is dealt with. Everybody has some familiarity with it. Probably the most surprising feature of a driven oscillator is the way in which a constant periodic driving force produces very different results, depending on its frequency. If the driving frequency is made close to the natural frequency, then the amplitude can be made very large even with quite small excitation forces.

For the analytical description of resonance we will use the well known harmonic oscillator. We consider a damped mass-spring system, whose behaviour at resonance is usually used in literature as a model for many real systems [21,22,23].

Although a mass-spring system has at first sight very little in common with a silicon bridge resonator, the nature of vibration of both systems is identical and we can use the resonance characteristics of the one to describe the characteristics of the other.

Finally we present an analytical method for calculating the basic resonance frequency of a clamped-clamped beam. It can be applied to the fabricated silicon resonator bridges.

2.1. Working principle of a thermally driven resonator

The resonator bridges are made of low-doped n-type silicon with two Boron-implanted U-shaped resistors and a thin (1500\AA) SiO_2 insulating oxide layer on top. To give the reader an idea of dimensions, a typical bridge measures $700 \times 50 \times 5\mu\text{m}$ ($L \times W \times T$). When applying a voltage to one of the resistors, a temperature increase due to the power dissipation in the resistor is observed. The bridge surface, where the resistor is located, will heat up more than the bridge bottom, thus a temperature gradient is established. Both the temperature gradient in the silicon and the different thermal expansion coefficients of silicon and the SiO_2 film cause stress in the bridge, and consequently a bending moment. This results in a very small deflection. If now the voltage applied across the resistor is periodic, the bridge starts oscillating, provided that the excitation frequency is equal to the bridge's natural resonant frequency. The amplitude of the vibration depends on the quality factor of the system.

Because the heating effect of a periodic electrical potential applied across a resistance varies as the square of the potential ($P=V^2/R$), the drive signal must either be half the resonant frequency of the bridge

$$(V_0 \sin \omega t)^2 = \frac{1}{2} V_0^2 (1 - \cos 2\omega t) \quad (2.1)$$

or else, a DC-bias must be superimposed

$$(V_1 + V_0 \sin \omega t)^2 = V_1^2 + 2V_0 V_1 \sin \omega t + V_0^2 \sin^2 \omega t \quad (2.2)$$

The latter technique is normally preferred for several reasons. If the motion of the bridge is sensed electrically with a piezoresistive resistor, and this electrical signal is used for excitation, it must have the same frequency as the excitation signal. For the characterization presented later, we compared excitation and detection signals in order to determine the resonance frequency. However electro-thermal drive with a DC-bias results in a loss of efficiency and an undesirable heating of the resonator element, caused by the first term in equation 1.2 [8]. If $V_1 > V_0$, the third term can be neglected.

As mentioned, the second diffused resistor is used for detecting the bridge motion. Silicon possesses piezoresistive characteristics, this means that mechanical stress in the material results in a change of resistivity. Given that the resistor is placed at a stress sensitive point on the bridge, it is submitted to a periodic stress. As a consequence, the resistance value of the resistor changes periodically. When supplied with a constant current, the mechanical oscillation of the bridge is transformed into an AC voltage with frequency equal to the vibration frequency.

As one would expect, the position of the resistors on the bridge plays an important role. Obviously, the piezoresistive detection resistor should be placed on the bridge where the oscillation causes the highest mechanical stress. This is also true for the excitation resistor. Therefore we derive the stress distribution in an oscillating bridge, taking as a basis the first oscillation mode. Throughout the whole report resonance refers to this vibration mode of the bridge, unless otherwise specified. It is characterized by only one amplitude maximum in the bridge centre.

The oscillation of a clamped-clamped beam is described with the following linear partial differential equation [24]:

$$EI_z \frac{\partial^4 y}{\partial x^4} + \rho A \frac{\partial^2 y}{\partial t^2} = 0 \quad (2.3)$$

E is Youngs modulus, I_z the moment of inertia of the beam, A its cross-section and ρ the density of the beam material. We do not show here the explicit solution; it can be found by starting with a solution $y(x,t)=Y(x)\cdot\exp(j\omega t)$ [25]. $Y(x)$ is the mode shape function of the resonance. With the boundary conditions, a solution for $y_1(x,t)$, the first or basic resonance mode, is obtained by solving the characteristic equation. The final result is [26]:

$$y_1(x,t) = A_1 \cdot Y_1(x) \sin(2\pi f_1 t) \quad (2.4)$$

with

$$Y_1(x) = \left[\cosh\left(\frac{\lambda_1}{L}x\right) - \cos\left(\frac{\lambda_1}{L}x\right) - 0.9825 \left(\sinh\left(\frac{\lambda_1}{L}x\right) - \sin\left(\frac{\lambda_1}{L}x\right) \right) \right] \quad (2.5)$$

where λ_1 is a constant characterizing the first mode shape ($\lambda_1=4.73$)

A_1 = Amplitude of the oscillation

x = Distance from the end of the bridge

L = Length of the bridge.

As we know the deflection equation $y_1(x,t)$, we can describe the longitudinal stress in the bridge, which is the dominant stress when oscillating. For equation 2.6 to be valid, we have to assume that the bridge body is uniform:

$$\sigma_{xx} = -E \cdot y \cdot y''_1(x,t) = -Ey \frac{\delta^2 y_1(x,t)}{\delta x^2} \quad (2.6)$$

σ_{xx} is the longitudinal stress in a homogeneous beam with rectangular cross-section submitted to pure bending. Pure bending excludes torsion as well as compression or elongation of the beam, and its neutral plane in the centre must neither be stretched nor compressed. y indicates the distance from the neutral axis, as shown in Figure 2.1. Consequently, the stress has a maximum at the top and bottom surface of the beam and is 0 at $y=0$, the neutral axis.

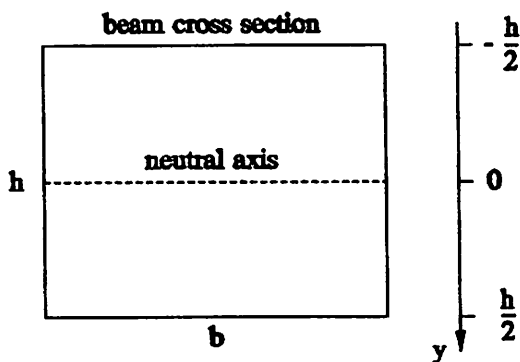


Fig. 2.1: Cross-section through a beam with width b and thickness h .

Substituting equation 2.5 into equation 2.6 leads to a stress equation that is applicable to the bridges:

$$\sigma_{xx,1} = -yEA_1\alpha^2 [\cosh(\alpha x) + \cos(\alpha x) - 0.9825 (\sinh(\alpha x) + \sin(\alpha x))] \quad (2.7)$$

with $\alpha = \lambda_1/L$.

$\sigma_{xx,1}$ describes the stress distribution at the maximum amplitude of the oscillating bridge in terms of x , the distance from the end of the bridge. The factors y , E , A_1 and α are not important in this case, as we are only interested in a relative stress distribution. Figure 2.2 plots the maximum relative stress for a bridge with length L .

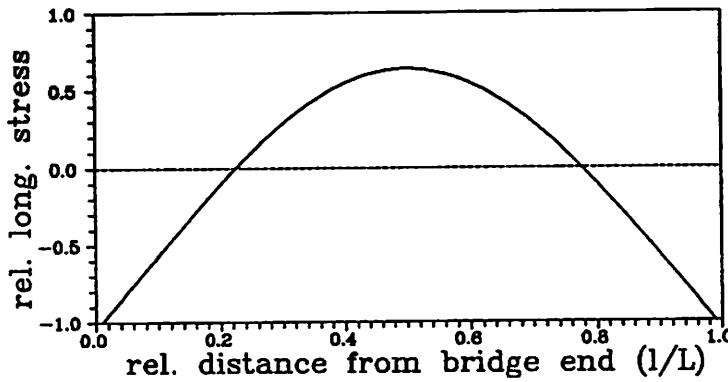


Fig. 2.2: Stress distribution in an oscillating bridge.

Consequently the best place for the resistors is either in the centre or close to the ends. In any case the two points with virtually zero stress, situated at about 22% of the bridge length, should be avoided.

2.2. Forced Vibration of a mechanical mass-spring system

We consider a damped harmonic oscillator, excited by a force of varying frequency. The form of the response is characterized by two quantities, a resonance frequency ω_0 and a quality factor Q . Together they characterize the properties of the oscillator. Our example, the well-known mass-spring system, is modelled by a mass m suspended by a spring of constant k . The damping is assumed to be linear with the velocity, expressed by the damping factor c . A sinusoidal driving force $F = F_0 \sin(\omega t)$ is applied. Then the equation of motion, in the form $m \ddot{x} + c \dot{x} + kx = \text{net force}$, is

$$m \ddot{x} + c \dot{x} + kx = F_0 \sin(\omega t) \quad (2.8)$$

Making $k/m = \omega_0^2$, $c/m = 2 \cdot n$ and $f = F_0/m$, this can be written as

$$\ddot{x} + 2n\dot{x} + \omega_0^2 x = f \sin(\omega t) \quad (2.9)$$

Before we discuss equation 2.9 in detail, let us consider the situation qualitatively. If the oscillator is excited with an impulse and then left to itself, it will oscillate, but due to the damping forces, the oscillation will die out. The frequency of this damped free oscillation, we assume here, is close to

the natural resonance frequency of the system. A periodic driving force will, however, try to impose its own frequency. We must expect, therefore, that the actual motion in this case is some kind of superposition of the two oscillations, the free and forced one. Indeed the mathematical solution of the motion equation 2.9 is the simple sum of a homogeneous solution χ_1 and a specific solution χ_2 . The initial state, in which the two types of motions are both prominent, is called the transient. χ_1 is the solution to

$$\ddot{\chi} + 2n\dot{\chi} + \omega_0^2\chi = 0 \quad (2.10)$$

Equation 2.10 represents exactly the above case of damped free oscillation. For $n < \omega_0$ a solution can be found

$$\chi_1(t) = A e^{-nt} \sin(\sqrt{\omega_0^2 - n^2} t + \alpha) \quad (2.11)$$

where A and α , the amplitude and phase lag respectively, are determined by the initial conditions. We do not derive this solution explicitly here, it is obtained with a general solution $\chi = A \cdot \exp(j(\omega t + \alpha))$.

χ_2 is a specific solution to equation 2.9. We shall now assume the following solution

$$\chi_2(t) = \text{Im} (B e^{j(\omega t - \varphi)}) \quad (2.12)$$

With this assumption we obtain

$$\begin{aligned} \chi_2(t) &= B \sin(\omega t - \varphi) \\ \dot{\chi}_2(t) &= B \omega \cos(\omega t - \varphi) \\ \ddot{\chi}_2(t) &= -B \omega^2 \sin(\omega t - \varphi) \end{aligned} \quad (2.13)$$

If we substitute from equation 2.13 into equation 2.9, we get the following conditions

$$\begin{aligned} B(\omega_0^2 - \omega^2) - f \cos \varphi &= 0 \\ 2nB\omega - f \sin \varphi &= 0 \end{aligned} \quad (2.14)$$

From 2.14 we find

$$\begin{aligned} B &= \frac{f}{\sqrt{(\omega_0^2 - \omega^2)^2 + 4n^2\omega^2}} \\ \tan \varphi &= \frac{2n\omega}{\omega_0^2 - \omega^2} \end{aligned} \quad (2.15)$$

The complete solution for equation 2.9, including homogeneous and specific solution, can thus be written as

$$\chi(t) = A e^{-\pi t} \sin(\sqrt{\omega_0^2 - n^2} t + \alpha) + B \sin(\omega t - \varphi) \quad (2.16)$$

The first term in equation 2.16 describes the transient state, while the second characterizes the stable state. The transient response of the system consists of a sinusoidal wave with attenuating amplitude. After some time, depending on the damping constant c , it will disappear and only a stable oscillation remains. As expected, the frequency of the vibration corresponds to the excitation frequency. We are aware that the vibration frequency ω here is not related to the natural frequency ω_0 of the system. Note that where there is no ambiguity, such as here, we refer to ω as "frequency" rather than "angular frequency".

From the stable state of equation 2.16 we can derive the condition of resonance, where the amplitude B has a maximum and the phase lag changes.

Resonance frequency

The amplitude B in equation 2.15 can be written as

$$B = \frac{B_0}{\sqrt{\left(1 - \frac{\omega^2}{\omega_0^2}\right)^2 + 4\left(\frac{n}{\omega_0}\right)^2 \left(\frac{\omega}{\omega_0}\right)^2}} \quad (2.17)$$

B_0 is the static displacement of the oscillator caused by the force F

$$B_0 = \frac{f}{\omega_0^2} = \frac{\frac{F}{m}}{\frac{k}{m}} = \frac{F}{k} \quad (2.18)$$

To simplify equation 2.17, we substitute as follows

$$\beta \equiv \frac{B}{B_0} \quad \zeta \equiv \frac{n}{\omega_0} \quad \lambda \equiv \frac{\omega}{\omega_0} \quad (2.19)$$

where β is the quotient of dynamic amplitude and static deflection. In doing so, we finally obtain a "normalized" amplitude of

$$\beta = \frac{1}{\sqrt{(1 - \lambda^2)^2 + 4\zeta^2\lambda^2}} \quad (2.20)$$

The dependence of β upon the frequency is shown in Figure 2.3. At resonance β has a maximum. To find it, we derive

$$\frac{d}{d\lambda}((1-\lambda^2)^2 + \zeta^2\lambda^2) = 0 \quad (2.21)$$

$$\lambda_{res.} = \sqrt{(1-2\zeta^2)} \quad (2.22)$$

or, expressed in terms of the excitation frequency ω

$$\omega_{res.} = \omega_0 \sqrt{(1-2\zeta^2)} \quad (2.23)$$

It can be seen that the "forced" resonant frequency of the system is smaller than its natural resonant frequency. For most cases of practical interest, however, the difference between $\omega_{res.}$ and ω_0 is negligibly small ($\rightarrow \zeta \ll 1$, we assume thus that the damping of our system is small. For systems where the damping medium is air and the internal friction is small, this assumption is practically always valid).

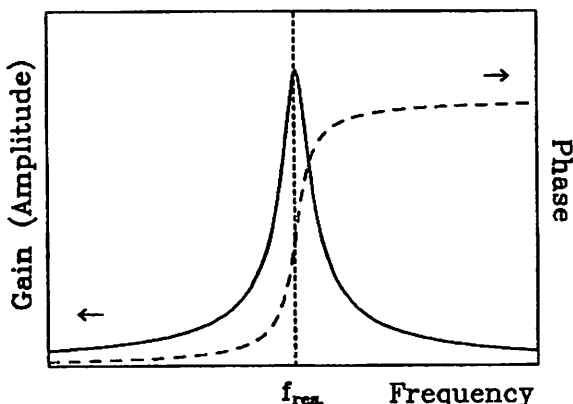


Fig. 2.3: Gain and phase lag of an harmonic oscillator around resonance.

Resonance amplitude

When substituting λ by $\lambda_{res.}$ in equation 2.20, we obtain for $\beta_{res.}$ the "normalized" amplitude at resonance

$$\beta_{res.} = \frac{1}{\sqrt{4\zeta^4 + 4\zeta^2(1-2\zeta^2)}} = \frac{1}{2\zeta\sqrt{1-\zeta^2}} \quad (2.24)$$

If $\zeta \ll 1$:

$$\beta_{res.} = \frac{1}{2\zeta} \equiv Q \quad (2.25)$$

Q is the quality factor of the system at resonance.

Phase lag

Let us write the phase in equation 2.15 as follows:

$$\varphi = \arctan \frac{2\zeta\lambda}{(1-\lambda^2)} \quad (2.26)$$

At resonance, when $\lambda \approx 1$ (we assume that $\omega_{res} \sim \omega_0$), the argument of the tangent becomes infinity, thus the phase lag is 90° . However, when considering the exact expression of the resonance frequency, it can be seen that φ_{res} is slightly less than 90° :

$$\varphi_{res.} = \arctan \frac{2\zeta\lambda_{res.}}{(1-1+2\zeta^2)} = \arctan \frac{\sqrt{1-2\zeta^2}}{\zeta} \doteq \arctan \frac{1}{\zeta} \quad (2.27)$$

The last simplification is valid again if $\zeta \ll 1$. In Figure 2.3 both the amplitude (gain) and the phase lag of the damped harmonic oscillator around resonance are plotted. For low frequencies, the phase lag is very small ($\varphi=0$ for $\omega=0$), and it increases continuously with higher frequencies. When passing through the resonance frequency, the phase lag is 90° . For higher frequencies it increases further until reaching 180° (in the limit $\omega \rightarrow \infty$). The total phase shift is thus 180° .

For the mass-spring system this means that at low frequencies the response is in phase with the excitation. At resonance, the mechanic system follows the excitation with a phase lag of 90° and for higher frequencies the system oscillates 'against' the excitation with a lag of 180° .

Quality factor Q

The resonance state is characterized by two parameters, the resonance frequency and the quality factor Q. As mentioned, Q is defined as the quotient of dynamic amplitude at resonance and static displacement

$$Q = \beta_{res.} = \frac{B_{res.}}{B_0} = \frac{\text{dynamic Amplitude (caused by } F \sin \omega t \text{)}}{\text{static displacement (caused by } F \text{)}} \quad (2.28)$$

For practical applications it is sometimes difficult to measure the static deflection of a system and/or its amplitude at resonance. A method that is usually employed, and included in most of the electrical gain/phase measurement equipments, is the calculation of Q directly from the gain/frequency plot, as shown graphically in Figure 2.4.

Q is obtained by dividing the resonance frequency by the width of the peak at an attenuation of 3dB ($1/\sqrt{2}$). Equation 2.29 can be proven to coincide with equation 2.28. The proof, that is not shown here, is carried out with the help of the expressions found for β , $B_{res.}$, λ and $\lambda_{res.}$

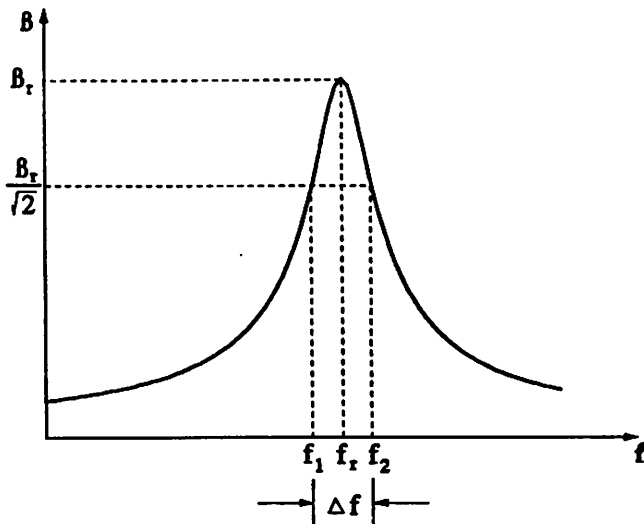


Fig. 2.4: Resonance peak with the 3dB frequencies marked for calculating the Q-factor.

$$Q = \frac{f_{res.}}{\Delta f} \Big|_{\beta = \frac{1}{\sqrt{2}} \beta_m} \quad (2.29)$$

The important results of this derivation are first the gain/phase characteristics around resonance, and second, the definition of the quality factor and a practical way of measuring it.

The derived gain/phase characteristics can be found in many mechanical harmonic resonant systems, even if their mathematical description differs from the one of the spring-mass system.

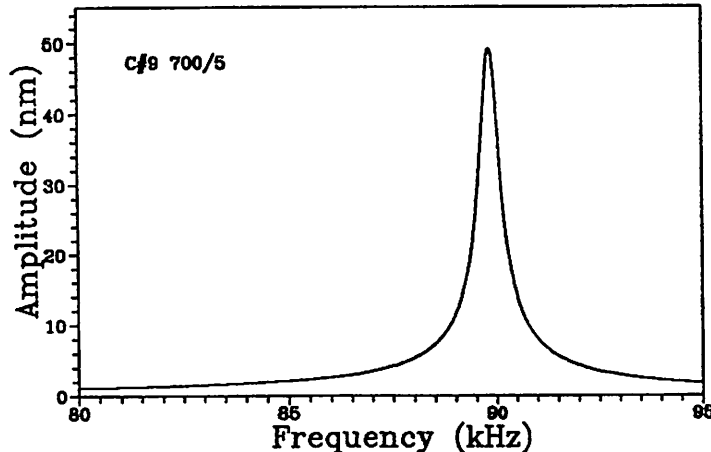


Fig. 2.5: Amplitude spectrum of a 700 μ m long resonator bridge.

As an example, Figure 2.5 shows the amplitude versus frequency of a driven bridge resonator (the resonator is a harmonic system, thus a sinusoidal force produces a sinusoidal response!).

The peak can be seen clearly, and from the resonance frequency of 89.83kHz and the given peak width of 460Hz at the 3dB frequency a quality factor of 195 is obtained.

2.3. Natural frequency of a clamped-clamped beam / Rayleighs method

Rayleighs method is a very effective analytical method for finding resonant frequencies of mechanical structures. It is commonly applied to beam and multi-mass systems, and requires that the deflection curve for the mode (whose natural frequency is to be calculated) is known, or can be estimated. Also called the energy method, its principle is based on assuming that the total mechanical energy (kinetic energy K plus potential energy U) of the system, is constant. An important limitation of this method is that it can theoretically only be applied to undamped systems. Therefore the application of Rayleighs method to a real system will always give an upper bound of the resonance frequency. For the following derivation we consider a resonator bridge as a clamped-clamped homogeneous beam made of silicon. We will calculate the fundamental resonant frequency, since it is the simplest case. The procedure is to assume that the maximum kinetic energy of the bridge at resonance equals the maximum potential energy.

The potential energy of the beam is determined by the work done on the beam which is stored as elastic energy. Letting M be the bending moment and θ the slope of the elastic curve, the work done is equal to

$$U = \frac{1}{2} \int M d\theta \quad (2.30)$$

For small deflections of the beam ($\theta \ll 1$), the following geometric relations, also illustrated in Figure 2.6, are assumed to hold

$$\begin{aligned} \theta &\approx \sin\theta = \frac{dy}{dx} \\ \frac{1}{R} &= \frac{d\theta}{dx} = \frac{d^2y}{dx^2} \end{aligned} \quad (2.31)$$

In addition to these equations we have, from the theory of beams, the flexure formula:

$$\frac{1}{R} = \frac{M}{EI} \quad (2.32)$$

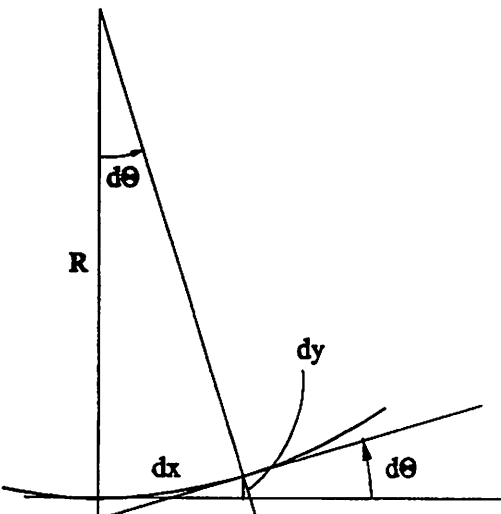


Fig. 2.6: Graphic illustration of equation 2.31.

where EI is the flexural rigidity of the beam, and R is the radius of curvature. $I=b \cdot h^3/12$ is the moment of inertia of the beam, with b and h the beam width and the thickness respectively. Substituting for $d\theta$ and $1/R$, U may be written as

$$U = \frac{1}{2} \int_0^L \frac{M^2}{EI} dx = \frac{1}{2} \int_0^L EI \left(\frac{d^2y}{dx^2} \right)^2 dx \quad (2.33)$$

where $y=y(x,t)$ represents the deflection of the beam.

The kinetic energy K of the beam is defined as

$$K = \frac{1}{2} \int_0^L y^2 \cdot \rho A(x) dx = \frac{1}{2} \int_0^L y^2 \cdot \rho b h dx \quad (2.34)$$

ρ is the density of the beam material, b and h the beam width and thickness respectively, $A(x)$ the beam cross-section and $\dot{y}=\dot{y}(x,t)$ the beam velocity.

For a specific vibration mode n we obtain the following expressions for deflection and velocity

$$\begin{aligned} y_n(x,t) &= Y_n(x) \sin(\omega_n t + \alpha_n) \\ y''_n(x,t) &= Y''_n(x) \sin(\omega_n t + \alpha_n) \\ \dot{y}_n(x,t) &= \omega_n Y_n(x) \cos(\omega_n t + \alpha_n) \end{aligned} \quad (2.35)$$

$Y_n(x)$ is the mode shape introduced in subsection 2.1. Substituting from equation 2.35 into equations 2.33 and 2.34, results in the following expressions for K and U

$$\begin{aligned} U &= \frac{1}{2} \int_0^L EI [Y''_n(x)]^2 \sin^2(\omega_n t + \alpha_n) dx \\ K &= \frac{\omega_n^2}{2} \int_0^L \rho b h [Y_n(x)]^2 \cos^2(\omega_n t + \alpha_n) dx \end{aligned} \quad (2.36)$$

At the point of maximum deflection of the vibrating beam the potential energy is equal to the total vibrational energy T . $U_{\max}=T$. A quarter cycle later, the maximum energy K_{\max} equals the total vibrational energy. $K_{\max}=T$. Therefore by setting $U_{\max}=K_{\max}$, we finally get

$$\omega_n^2 = \frac{\int_0^L EI [Y''_n(x)]^2 dx}{\int_0^L \rho b h [Y_n(x)]^2 dx} \quad (2.37)$$

This is the so-called Rayleigh Quotient. It expresses the vibration frequency as a function of the mode shape. If the exact mode shape is unknown, an approximation can be taken instead.

For the fundamental vibration frequency ($n=1$) of a resonator bridge, we take the static displacement $y_{\text{stat}}(x)$ of a clamped-clamped beam, as a good approximation for $Y_1(x)$. It is calculated from [27]:

$$y_{\text{stat.}}(x) = \frac{\rho b h g}{24 E I_z} x^2 (x - L)^2 \quad (2.38)$$

Here b, h, L represent the width, thickness and length of the beam, ρ and E are density and Youngs modulus respectively, I_z is the moment of inertia of the beam and g is the earths gravitation.

Substituting $y_{\text{stat.}}(x)$ in equation 2.37, we finally obtain a fundamental resonance frequency:

$$\omega_0 = \frac{4.738^2}{L^2} \sqrt{\frac{EI}{\rho b h}} \quad \Rightarrow \quad f_0 = 1.03 \frac{h}{L^2} \sqrt{\frac{E}{\rho}} \quad (2.39)$$

Equation 2.39 is usually found in literature [26]. Note that the resonance frequency does not depend on the beam width (we have not mentioned it before, but this is only valid as long as $L \geq 10w$). Knowing thickness and length of a resonator bridge, its theoretical fundamental natural frequency can be calculated, using the appropriate values for E_{Si} ($1.4 \cdot 10^{11}$ N/m²) and ρ_{Si} (2328 kg/m³).

The limitations of Rayleighs method are evident from the derivation. Its approximation is one dimensional, neglecting shear, rotational, or any other three-dimensional effects. The displacement function $Y(x)$ must be assumed and is still unknown. Because of this assumption, normally only the frequency of the basic resonance mode is calculated.

Nevertheless, for finding a good approximation of the fundamental resonance frequency of a resonator bridge, Rayleighs method is an excellent analytical tool.

III Design

The design of the resonator bridges was guided by the objective that the thermal excitation principle applied to micromachined silicon bridges was to be studied and evaluated. From this starting-point we designed different bridges, varying the geometrical parameters such as length, shape, resistor position, etc, that were not fixed by the fabrication process. This resulted in a chip with 24 different bridges, that enabled comparisons to be made in order to find the most suitable bridge design in view of the future application in a resonant sensor.

As the design phase coincided with a project about piezoresistive acceleration sensors, and as both these accelerometers and the resonator bridges required very similar fabrication technologies, one maskset incorporating both projects was designed. The resonator chip and three different accelerometer chips were arranged together as one square chip. Although compatible, the fabrication processes differed slightly, which meant that wafers processed to obtain resonator bridges contained no functioning accelerometers, and vice versa. This had no influence on the devices, just the yield of working chips per wafer was decreased.

The maskset CNM024, in total 10 mask levels, contains 11x11mm large chips. Each chip is subdivided into one 5.5x5.5mm large resonator bridge chip and three accelerometer chips of the same size. In the next subsection only the mask levels required for the fabrication of the resonators are described. Also the different bridge designs are explained and the reason for their incorporation is justified.

3.1. Mask layers

The fabrication of the resonators required seven mask layers:

n-well implant	(L2, blue)
p ⁺ -implant	(L4, orange)
p-implant	(L3, red)
Opening contact windows	(L5, black)
Metallization	(L7, yellow)
Wet etch patterning	
Dry etch patterning	(L8, purple)

(Colours and numbers in parenthesis refer to the layout plot in Appendix A).

For defining accurately the thickness of the resonator bridges, we used a four-electrode electrochemical etch stop technique, as described in detail in the next section. However we give a short explanation of the principle of this technique here, to help in understanding the function of the different layers. Biasing silicon anodically with respect to the etching solution prevents it from being etched away. This effect was used for fabricating silicon membranes, from which the resonator bridges were finally etched. We implanted an n-well into a p-substrate wafer and made contact pads to both n-well and substrate. By applying an anodic potential to the well and a cathodic potential to the p-substrate, the substrate is etched while the well is untouched. In this way the substrate under the well can be etched away, creating a silicon membrane corresponding to the thickness of the well. This method of etching p-substrate is usually chosen for fabricating membranes, since the p-n-diode between well and substrate is reverse biased, and the current flowing through the diode is very small.

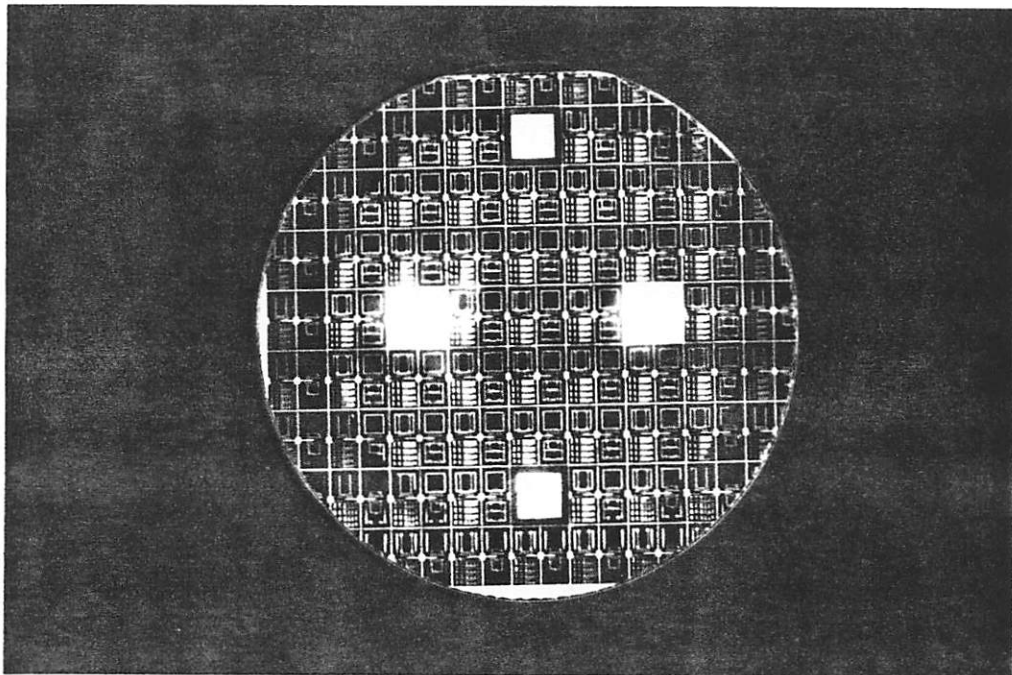


Fig. 3.1: Photograph of a complete device wafer containing accelerometer and resonator chips.

To be effective across the whole wafer, the electrochemical etch-stop requires a *constant* potential of both well and substrate across the complete wafer. This implies metallic contacts to the two types of silicon. Our approach consisted of implanting one coherent n-well, leaving substrate islands on every chip. The n-well extended across the whole wafer and was thus automatically interconnected.

Mask layer two contains the n-well pattern. The substrate islands were connected together by a metal grid along the scribe lanes extended over the whole wafer. In this way n-well and p-substrate were

biased with just one metal contact each. For symmetry reasons, however, we placed four contact pads, two for the substrate and two for the well, symmetrically spread over the wafer, as seen in the photograph in Figure 3.1.

Obviously the contact chips have the same size as the device chips. Both p-substrate contact chips, visible on the left and the right, are completely metallized and touch the metal grid on the scribe lines of the adjacent device chips. The n-contact chips, however, are isolated from the metal grid. There the contacts are made directly to the underlying n-well. Moreover, besides their function in the electrochemical etch-stop process, the p-substrate contact chips contain the double sided alignment markers that are necessary when photolithography processes are performed on both sides of the wafer (see also subsection 4.1.).

Mask layers three and four contain the pattern for the piezoresistive resistors and their highly doped contact areas, and *layers five and seven* are for opening contact windows in the passivation oxide and for the patterning of the subsequently deposited metal film.

The wet etching was done from the backside of the wafer. Therefore *mask layer six*, which contains the wet etch opening pattern, had to be aligned to structures on the frontside of the wafer. This mask, therefore, contains double sided alignment markers on the contact pad chips.

Due to the anisotropic etching characteristics of the KOH etchant used, the final membrane sizes come out smaller than the initial wet etch openings (by a factor $(\tan 54.7^\circ)^{-1} = 1/\sqrt{2}$ on each side). For example, the wet etch opening for a $700\mu\text{m}$ long bridge should have a length of $(700+2 \cdot 300/\sqrt{2})\mu\text{m} \approx 1124\mu\text{m}$, where $300\mu\text{m}$ corresponds to the etching depth. However the etching with KOH is not completely anisotropic, and a slight misalignment between the (110) oriented wafer flat and the (110) orientation on the etching mask can reduce even more the anisotropy factor. For this reason we added a distance of only $200\mu\text{m}$ instead of $(300/\sqrt{2})\mu\text{m} = 212\mu\text{m}$ to each side of the wet etch openings.

In addition, to facilitate the separation of the final chips, $200\mu\text{m}$ wide line-shaped wet etch openings were drawn along the scribe lines of the chips. When etched, about $140\mu\text{m}$ deep V-shaped breaking grooves were produced. With these grooves, single chips were easily separated by breaking, without damaging the fragile bridge structures.

Finally, mask layer eight contains the pattern corresponding to the membrane area to be dry etched to free the silicon bridges. In section 1.1. we commented that the dry etch process was not completely anisotropic. Since the experimentally found value of $2\mu\text{m}$ of horizontal undercutting at a vertical etch depth of $5\mu\text{m}$ could be tolerated, the dry etch pattern were drawn as projected.

3.2. Mask layout

In Figure 3.2, that shows a schematic plot of the mask layers on the frontside of the chip, it can be seen that the resonator bridges are located in 12 opening holes. For comparison, a photograph of a processed chip is added.

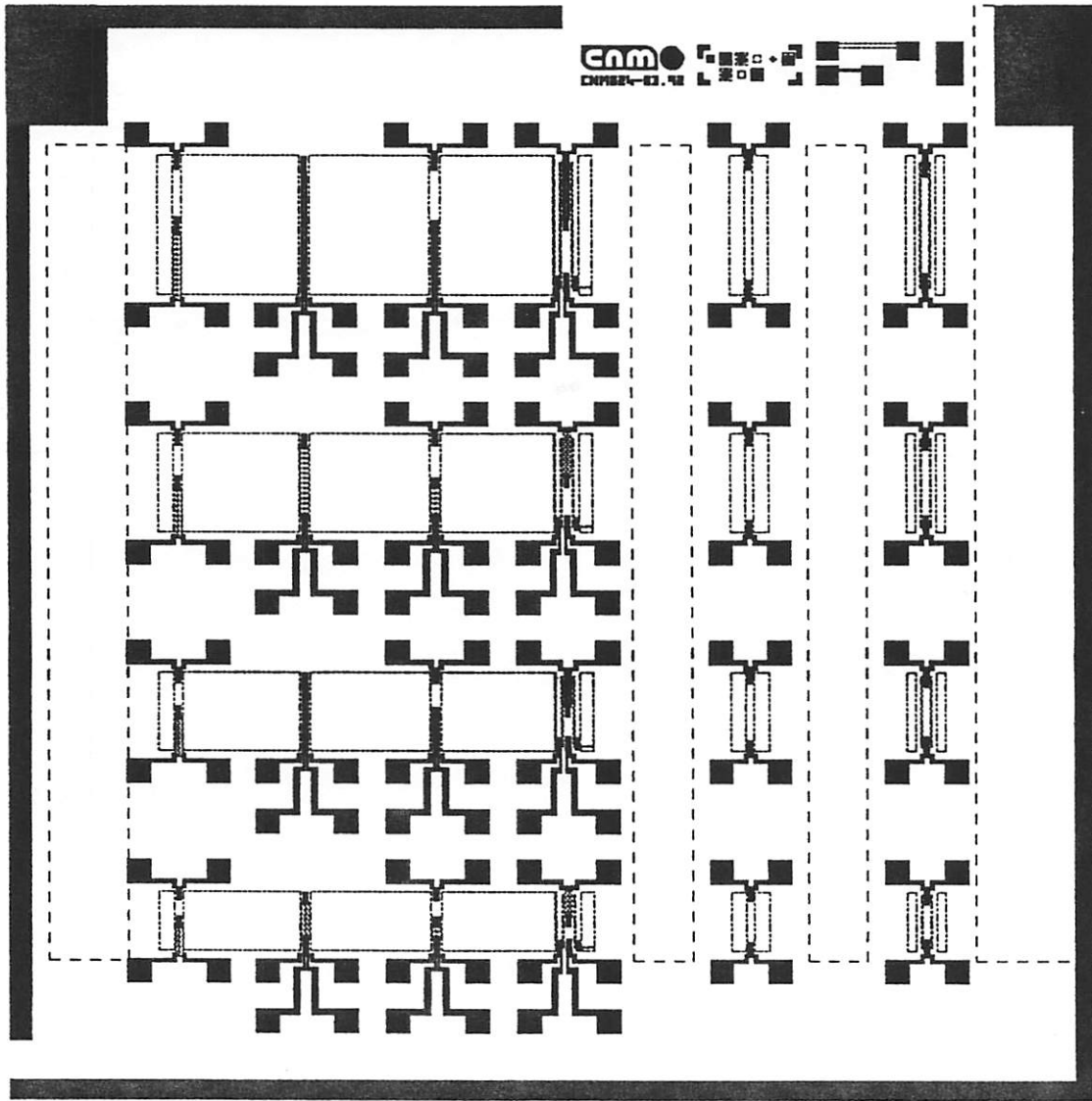


Fig. 3.2: Plot of the mask layers on the frontside of the chip (Filled black pattern: aluminium).

The large distances between adjacent opening holes and between opening holes and the frame of the chip, 700 and 750 μm on the chip surface respectively, were designed on purpose. Due to the V-shaped etching walls, the substrate area on the wafer backside is smaller than on the wafer frontside. When bonding the final chips to a glass substrate, the bond quality depends, amongst other things, on the area to be bonded. A larger bond area makes the bond process easier. For this reason a wider chip frame is desireable.

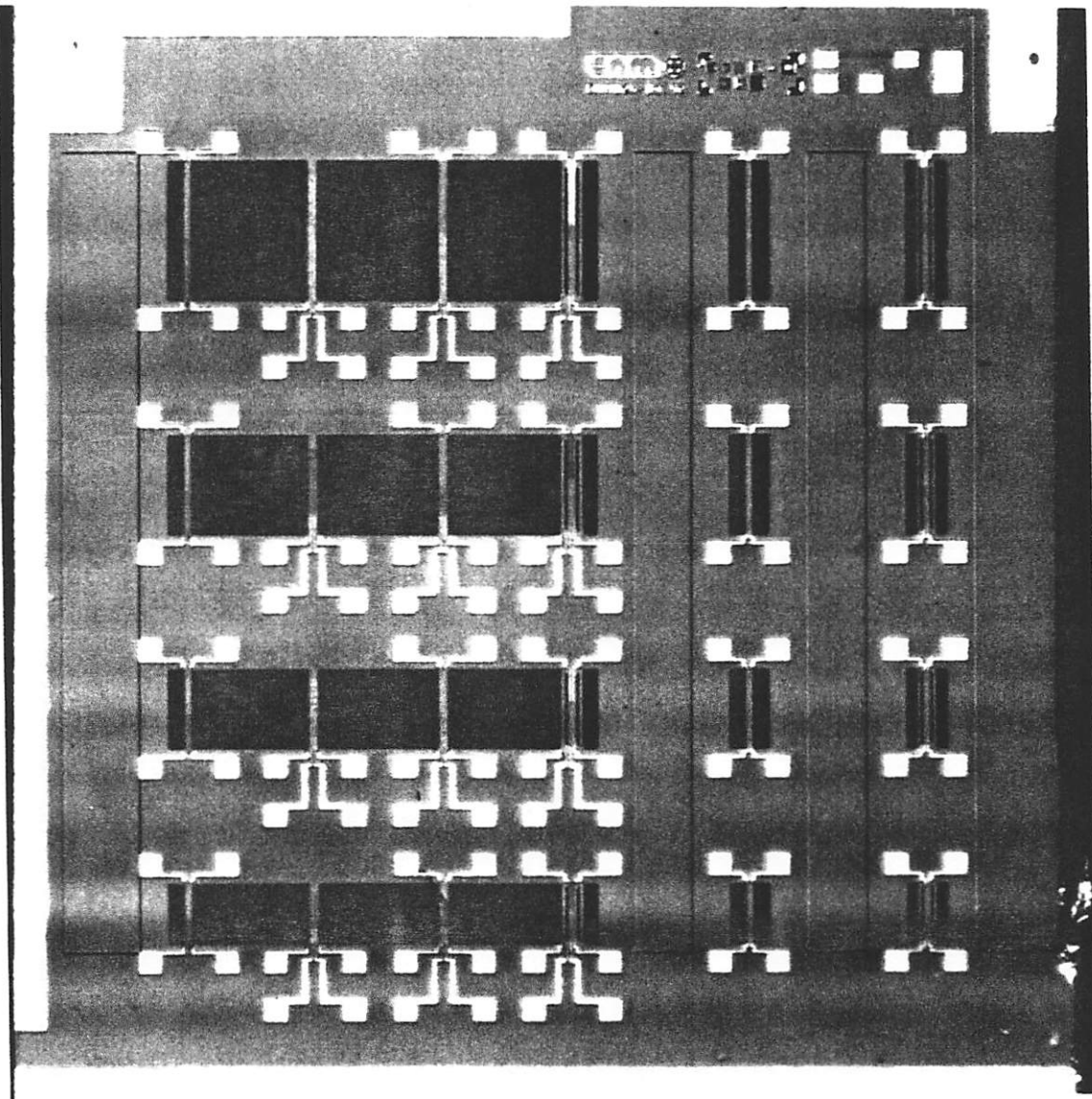


Fig. 3.3: Photograph of a processed resonator chip.

Four groups of bridges with different length, 300, 400 500 and 700 μ m, were designed. Theoretical resonance frequencies for a given thickness of 5 μ m vary from approximately 80kHz for a 700 μ m long bridge up to 430kHz for a 300 μ m long bridge. The short designs were ineffective, the resonance frequencies for the 300 and 400 μ m long bridges could hardly be detected and measured. Widths vary from 40 to 50 μ m for single bridges. The triple bridges measure 24-48-24 and 20-40-20 μ m respectively. In each row there are six bridges, all distinguished by their shapes and resistor arrangements.

The resistor arrangement strongly influences the drive and the sensing efficiency. As shown in Figure 2.2 in section two, the longitudinal stress distribution in a clamped-clamped bridge vibrating in its first resonance mode has a parabolic shape, with maxima at both ends and in the centre. The two points with virtually zero stress, are situated at about 22% from the bridge ends. For efficient excitation and detection, the resistors should be placed either at the ends or in the centre, avoiding

the two stress minimum points. In our design, the resistors at the bridge extremes occupy approximately 10 to 15% of the total bridge length, depending on the length of the bridge. Most of the resistors are U-shaped, except some which have the shape of an M. These are exclusively located in the centres.

U-shaped resistances with a narrow connection link between the two parallel 'arms' of the U, are the most advantageous design with respect to the piezoresistive characteristics. As they are orientated in the bridge, (and thus also in the stress) direction, the longitudinal piezoresistive coefficient

$$\pi_u = \frac{1}{2}\pi_{44} \quad (3.1)$$

is valid [28]. Given a piezoresistive coefficient of $\pi_u \sim 40 \cdot 10^{-12}$ cm²/dyn for p-doped silicon (concentration 10^{19} cm⁻³), a Gauge factor of approximately 70 results. Although not extremely high, this value is larger than, for example, the Gauge factor of polysilicon (given the same impurity type and the same orientations of resistor and stress), which is in the range of 20..30.

Next the different bridge types are described, starting from the bridges on the left side.

Bridge type one contains one resistor at the end and another one in the centre. The centre resistor is connected by p⁺-implant lines. Both resistors can either be used for excitation or for detection.

Bridge type two contains both resistors at the ends of the bridges. However the contact pads are placed at one end of the bridge. This arrangement is important in view of a future resonant accelerometer, where a resonant bridge is coupled to a seismic mass and 'access' to the resistors will only be possible from one side. Connections to the resistor opposite to the contact pads are either made by aluminium lines (400, 700μm long bridges) or by p⁺-implanted lines (300, 500μm long bridges). The power dissipation in the aluminium tracks is much lower, although their influence on the resonance frequency of a thermally driven bridge - an additional 1μm thick aluminium layer with a thermal coefficient of expansion very different from that of silicon - is greater than that of p⁺-implanted connections.

Bridge type three comprises three resistors, where the one in the centre can either be used for measuring the temperature of the driven bridge or for excitation/detection.

Bridge type four consists of a so-called triple bridge with a central bridge twice as wide as the outer two [1]. The coupling zones, where the three bridges are joined together, each occupy 5% of the total bridge length.

This bridge has three different basic longitudinal oscillation modes. Either the three bridges oscillate

in phase, or the central bridge does not vibrate while the outer bridges oscillate at a phase of 180° . In the third mode the two outer bridges oscillate at a phase of 180° with respect to the central bridge. In this mode both bending and shearing forces at the common mounting points are cancelled out and very little vibrational energy is coupled into the supporting frame at the end. As a consequence, the quality factor of this oscillation mode is higher than that of the other modes.

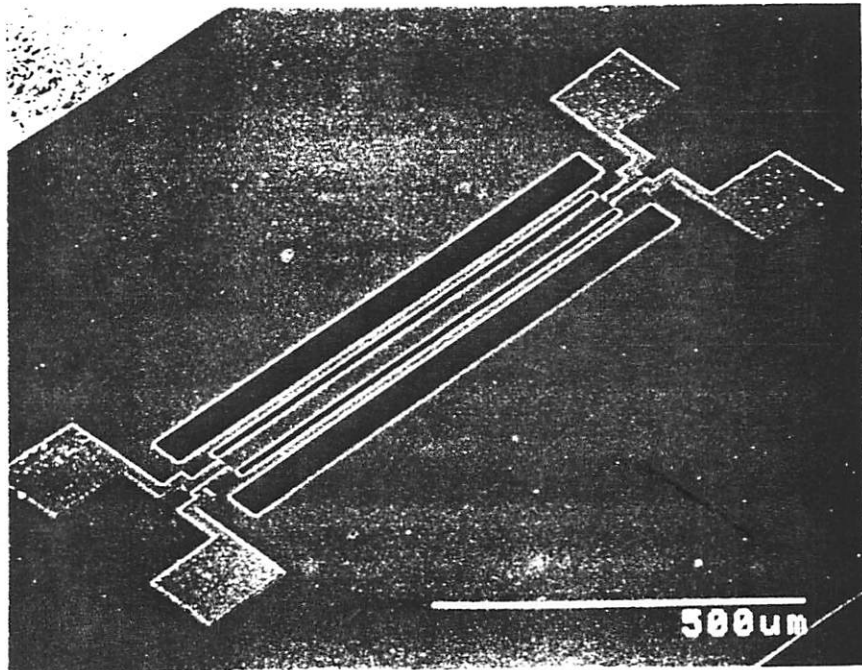


Fig. 3.4: SEM photograph of a triple bridge (length $700\mu\text{m}$).

Satchell and Greenwood performed numerical resonance frequency simulations of a similar triple bridge in 1989 [2]. In contrast their design had a coupling zone at only one end of the bridge. However the results, that can be seen in Figure 3.5, can be transferred to our triple bridge design. Unfortunately we do not know the relative length of the coupling zone used in their simulation. Nevertheless the figure gives an indication of whereabout the resonance frequencies of the different modes are to be expected. As expected, they depend on the length of the coupling zones. The in-phase oscillation has the lowest resonance frequency, followed by the second and the third mode. For short coupling zones, the three resonance frequencies close to each other. FEM simulations revealed that by reducing the length of the coupling zones, the frequencies of the three modes converge [29]. The coupling zones should have a length of at least 5% of the total bridge length in order to monitor the different resonance frequencies.

In our design two resistors are placed on the central bridges and one on the outer bridge. They can be used for both excitation and detection.

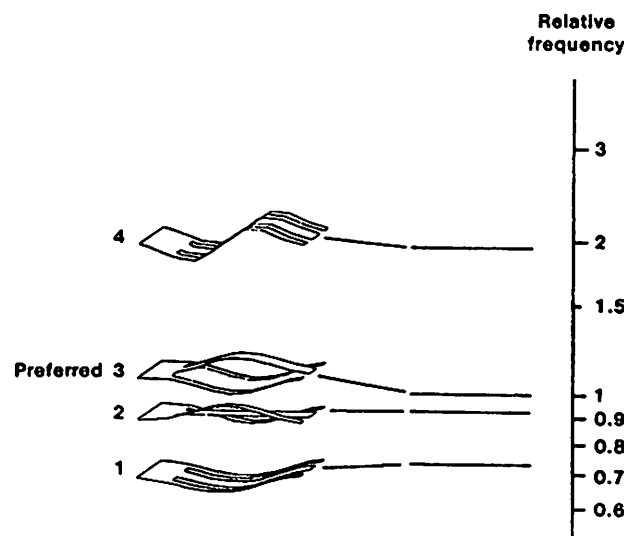


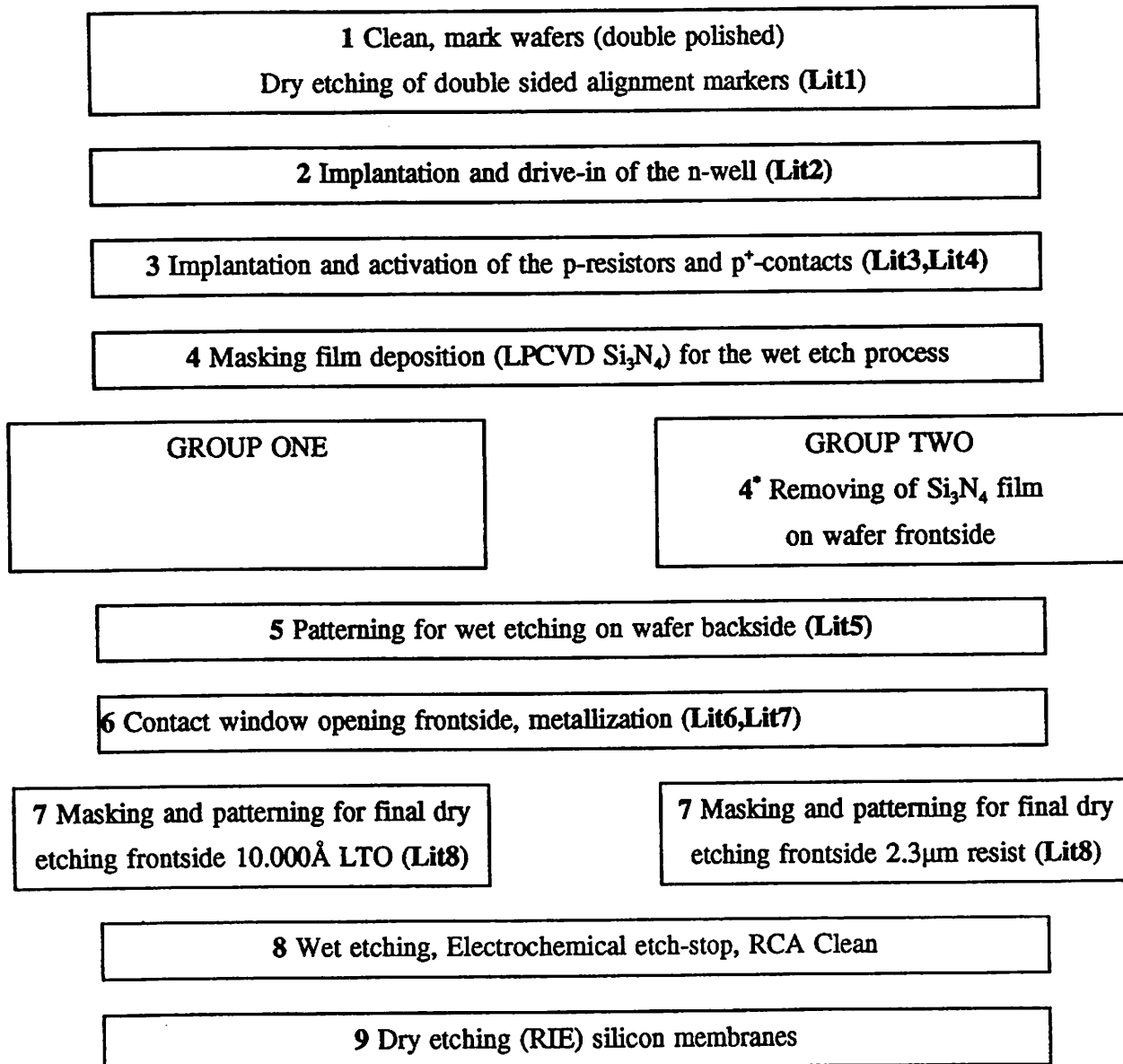
Fig. 3.5: Resonant modes and relative frequencies of a triple bridge (from [3]).

Bridge types five and six are identical to bridges two and four. However they are in a single opening hole to avoid possible self excitation effects of neighboured bridges. This may occur when exciting one of the adjacent bridges located in a large opening hole. This effect was, however, not observed during measurement.

IV Silicon Processing

4.1. Process flow

The fabrication process can be divided into two parts: First, the wafers passed through the standard IC fabrication line where the different masking processes, implantations, annealings, etc. were performed. The smallest mask pattern had a size of $5 \times 5 \mu\text{m}$, namely some contact window openings. Next the micromechanical processes were carried out, wet anisotropic etching with a four-electrode electrochemical etch-stop technique, and finally a silicon trench dry etching process. One batch of twelve wafers - Run 280-RES - was processed. The devices were fabricated entirely at CNM. A simplified version of the process flow chart - the detailed one is in Appendix B - is shown.



**10 Removal SiO₂ rests dry
etching mask: 10% HF solution**

**10 Removal photoresist rests dry
etching mask: Barrel Asher**

1 The starting material was double polished, 300 μm thick, (100) oriented 4" wafer (Boron doped, $\mathbf{q}=12..18 \Omega\cdot\text{cm}^{-1}$) from Virginia Semiconductors. After marking and cleaning, the double sided alignment markers were dry etched on the wafer frontside. These markers are located in two chips, whose positions on the mask were defined by the optics of the mask aligner. Layer number eight (dry etching) contained the etch pattern. The etched depth was 2000Å and photoresist was used as the masking material. This 2000Å high step in the substrate, which remains during subsequent oxidation, is deep enough to be recognized by the infrared system of the double sided mask aligner.

2 The n-well had to meet two conditions. When using a four electrode electrochemical etch-stop technique, the etching stops close to the physical p-n junction. Thus the n-well depth corresponds approximately to the final thickness of the resonators.

Second, the conductivity of the well influenced the correct working of the electrochemical etch-stop. During the etching, the p-substrate-n-well diode is reverse biased. Since the potential to the well is applied only via two contact pads, a constant potential distribution depends strongly on the conductivity of the well. In the case of diode leakage currents, a highly resistive well could cause voltage drops. As a consequence of this, the potential away from the contact pads would shift towards more cathodic values, and in the extreme case it would take the potential of the p-substrate. In these regions the well would not be protected anymore and the etching would not stop. Therefore the well conductivity must be high enough to avoid this effect.

We chose a well depth of 5 μm together with a surface concentration of approximately 10^{17} cm^{-3} . This value was low enough for subsequent integration of the resistors. Simulations with Suprem III, see also subsection 4.3, provided the implant and drive-in parameters.

3 Two different sheet resistance values, of 100 and 200 Ω/\square , respectively, were chosen for the resistors. Both implants resulted in a boron surface concentration higher than 10^{19} cm^{-3} . This was especially important for the resistors used for piezoresistive detection. At high impurity concentrations the temperature coefficient of the piezoresistive effect in silicon is very low.

During the annealing for electrical activation of the implants an oxide was grown, which in group one formed part of the final passivation layer, and in group two was the passivation layer on the resonator bridges. To minimize residual mechanical stresses in the bridges due to the compressive film of thermally grown SiO₂ on top, a thin film of 1500Å was chosen. Note that only this thin oxide isolates the aluminium from the substrate. For IC circuitry this solution would not be tolerable due to the very high 'to substrate' capacitance of metal pads or lines.

4, 4° and 5 An 1800Å thick LPCVD Si₃N₄ film was deposited and patterned on the wafer backside as masking material for the wet etching step. In this photolithography step, the photomask had to be aligned to a pattern on the opposite side of the wafer. The double sided mask aligner is equipped with an infrared light source. Since silicon is transparent to infrared light, the alignment pattern on mask and wafer can be matched. The process is monitored on a screen. Between the alignment pattern of wafer and mask there is a distance of one wafer thickness, in our case 300µm. The diffraction of IR-light that this causes, reduces the alignment precision. A best precision of 5µm is specified by the aligner manufacturer.

During the photolithography, an opaque plastic ring with a diameter of 80mm was placed on the mask. In this way a nitride ring at the border of the wafer was retained. The ring was necessary for the wet etch process, where the wafer was sealed in an etching chuck (also see Section Electrochemical Etching). If the round O-ring (diameter 85mm), that seals the interior of the chuck, fitted over patterned structures, the silicon under the ring would be etched away and etchant could enter the chuck. By protecting the area under the O-ring the problem could be avoided.

In group one the deposited nitride film together with the underlying oxide forms the final passivation layer sandwich on the resonator bridges. Resonance frequencies of bridges of group one were thus expected to be higher than calculated due to the tensile stress of the nitride layer. In group two the nitride layer on the frontside was removed.

6 After etching the contact windows, the wafers were metallized and patterned.

7 The mask for the final dry etching was deposited. In group one, we used a 1µm thick undensified LTO and in group two a 2.3µm thick photoresist film. Previous test runs revealed a ratio of LTO (photoresist) to silicon etch rates of about 15:1 (5:1), that means that at least 10µm of silicon could be etched with both masks. For greater depths, the resist mask deteriorates rapidly, because of the heating of the wafer during the process. The reason for using two different dry etching masking layers is obvious. It was not possible to mask wafers of group two, that had an oxide passivation film, with LTO, because, when removing the LTO after the dry etch process, the passivation oxide would also have been at least been partly etched.

8 During the anisotropic wet etching, the wafer was sealed in an especially developed etching chuck, protecting the side not to be etched. On this side the electrical contacts for the electrochemical etch-stop were made. In the next subsection the process is explained in more detail. The KOH solution used contained 40% weight KOH and had a temperature of 75°C. After the etching the wafers were cleaned in a hot HCl solution.

9 The membranes obtained in step eight were dry etched. A standard SF₆ process, as for the CNM

CMOS poly-etch was used. Although the process is not anisotropic, we found that the underetching for an etch depth of $5\mu\text{m}$ was not more than $2\mu\text{m}$. The bridge width were thus reduced by about $4\mu\text{m}$, which was acceptable.

10 Finally the remains of the etch mask had to be removed. The resist on wafers from group two were removed in a Barrel ash, while the remaining LTO on wafers of group one was etched in a 10% HF solution. Since this oxide was thin and of poor quality, the HF etch time required was short and no harm to the aluminium could be observed.

4.2. Electrochemical Etching

4.2.1 Principle

Among the recently developed micromachining techniques, the electrochemical etch-stop at a p-n junction is a very versatile tool for the fabrication of thin membranes with precise thickness control and high repeatability. In comparison with other techniques, low-doped stress free single crystal silicon can be used, which ensures very good mechanical properties. Moreover for micromechanical applications such as piezoresistive pressure sensors or accelerometers, the integration of diffused piezoresistors or even of IC-circuitry on membranes is possible.

A complete study of the electrochemical etch-stop was performed at CNM [30] and the process is being used now as a standard step for the fabrication of micromachined sensors. Nevertheless we will summarize the working principle of the electrochemical etching, as it was used as a basic tool for the fabrication of the resonator devices.

In 1970 Waggener [31] first reported the effect that, when applying a sufficiently anodic bias to silicon with respect to the etching solution, the etching could be stopped. He protected the wafer side where the electrical contact was applied with black wax. A simple piece of aluminium paper acted as an electrode in the etching solution, and the bias was directly applied between wafer and the aluminium electrode. While he used KOH, it was later demonstrated that the electrochemical etch-stop works with almost all anisotropic wet etchants [15,32,33,34]. Nowadays the working tools are more sophisticated, but the principle is still the same. Using only two electrodes, the silicon itself and an inert metal electrode in the etching solution, has an important drawback. The potential between the electrodes depends on the current through them. A large current will cause a potential drop, unless an ideal voltage source is used. With this setup it is thus difficult to maintain a constant bias between silicon and electrode. A common way to overcome this problem is the use of three electrodes controlled by a potentiostat, instead of two. Apart from the silicon, a reference and a counter electrode

are immersed into the etching solution. The potentiostat constantly adjusts the potential of the counter electrode in such a way that the reference electrode does not draw current. In this way the contact potential between reference electrode and etching solution is stable and the silicon can be biased with respect to the reference electrode. This configuration is commonly called a three electrode setup. Normally either a Hg/HgCl (Standard Calomel Electrode) or a Ag/AgCl are used as Reference Electrode. The Counter Electrode is usually an inert metal electrode, e.g. platinum. By applying a potential ramp between the silicon and the etching solution, an I/V graph can be obtained displaying the current between silicon and the etching solution as a function of the applied potential. At a certain potential the current drops sharply, indicating passivation of the silicon. For potentials anodic to this so called passivation potential (PP), the silicon etch rate slows down abruptly to negligible values [35]. This effect can be observed with both n- and p-doped silicon.

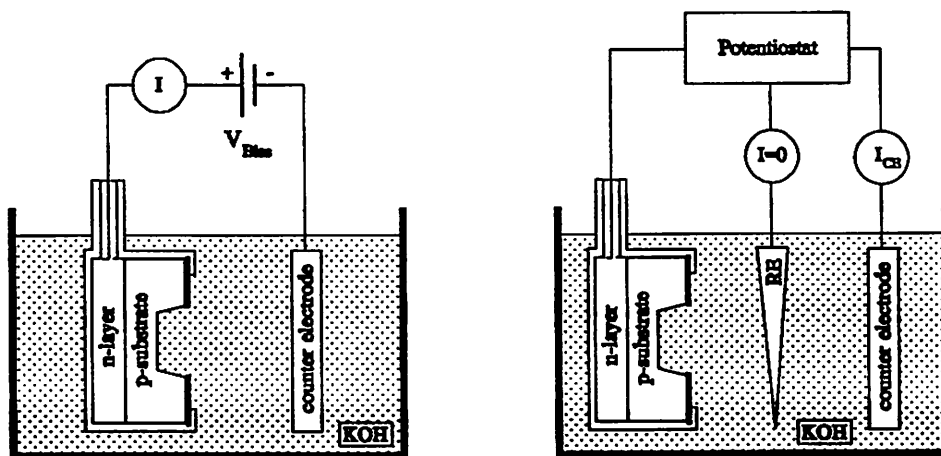


Fig. 4.1: Standard two (left side) and three electrode setup for electrochemical etching.

In Figure 4.2 we show such an I/V graph recorded with one of the device wafers before the etching. The peak shape, that looks like cut off, is due to the voltage source used for the sweep. Its maximum current is limited to 40mA, thus limiting the peak value.

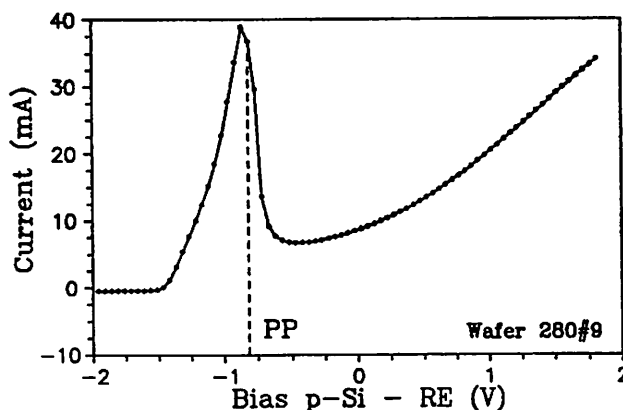


Fig. 4.2: The electrochemical I/V characteristics of p-type silicon in a 40% wt. KOH solution at 75°C.

From the Figure a PP for p-type silicon of about -0.8V results; we found a PP for n-type silicon of the same order.

It is known that this passivation is due to the growth of anodic passivation oxides [36,37], although the exact process is not yet fully understood. The passivation oxide explains the residual etch rates of electrochemically passivated silicon, which in KOH, TMAH and EDP are in the order of the etch rates of thermal SiO₂ [35].

A widely used process for fabricating thin membranes is the electrochemically controlled etching of a p-substrate wafer with an epitaxial n-layer. Ohmic contacts to the epitaxial layer are made directly on the wafer. During the etching the wafer is sealed in an etching chuck, only exposing the side to be etched to the etchant. On the protected side contact is made to the n-layer. It is kept at passivation potential with respect to the etching solution. The p-substrate, which is in direct contact with the solution, is automatically maintained at etching potential. This potential is also called open circuit potential (OCP), assuming that the whole potential applied drops across the junction. Once the entire p-substrate is etched away and the passivated n-layer is reached, the etching stops. In this way a well defined etch-stop at the p-n junction can be achieved, leaving a membrane corresponding to its depth. One inconvenience of the three electrode setup, is that the potential of the p-substrate is not well defined. In the ideal case it should take the potential of the etch solution, as a consequence of which the p-substrate - n-layer diode becomes reverse biased. In the case of diode leakage, however, the p-potential can shift. In the worst case, it can take the potential of the n-layer, thus passivation would occur. To avoid this undesirable effect, the p-substrate can be additionally biased with respect to the n-layer. Then both the potentials of p- and n-silicon are well defined with respect to the etching solution. This setup, shown in Figure 4.3, was firstly suggested by Kloeck et al. [38] and it is normally referred to as the four-electrode configuration.

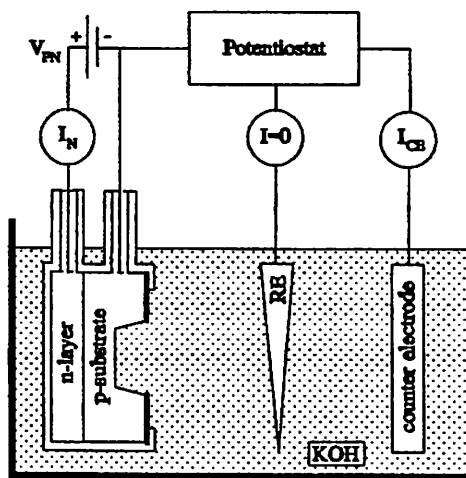


Fig. 4.3: Four-electrode configuration for electrochemical etching.

When etching electrochemically, the etching does not stop exactly at the physical p-n junction, but at some distance before it. That distance depends on the potential applied to the n-silicon. The more

anodic from the PP it is, the further away from the junction the etching stops. This behaviour is attributed to the influence of the space charge region of the junction [37], although the complete mechanism is not fully understood.

As mentioned, the n-layer is normally made from epitaxy on a p-substrate wafer. When using a four-electrode configuration, however, the question of how to contact the p-substrate arises. Either deep p-diffusions have to be made through the n-layer, or the wafer has to be contacted on the side which is etched. An elegant and new way to avoid this, is to define the n-layer by a diffusion or an implantation, as we did. First, selective n-areas can be fabricated, leaving access to the p-substrate. Moreover the depth of the n-layer can be adjusted easily, and several different depths can even be used on the same wafer.

4.2.1 Fabrication of the Resonator membranes

We used a four-electrode configuration as seen in Figure 4.3 with a potentiostat (Tacussel PTJ 24-1), a Reference (AgCl) and a Counter Electrode (Pt) (henceforth called RE and CE). The potential between RE and p-silicon was fixed by the potentiostat, and a voltage source biased the n-silicon. The etching chuck, made of propylene, allowed a wafer area of 8.5 cm in diameter to be etched. During the etching the interior of the chuck was kept under slight nitrogen overpressure to prevent leakage problems.

When etching with a potential of $V_n=0V$ with respect to the RE (above the passivation potential of about -0.8V), only the membranes in the neighbourhood of the contacts etch-stopped correctly. Further away from the contacts the membranes were thinner and even completely etched away. The reason, which is explained in subsection 3.2, can be attributed to the high sheet resistance of the n-well.

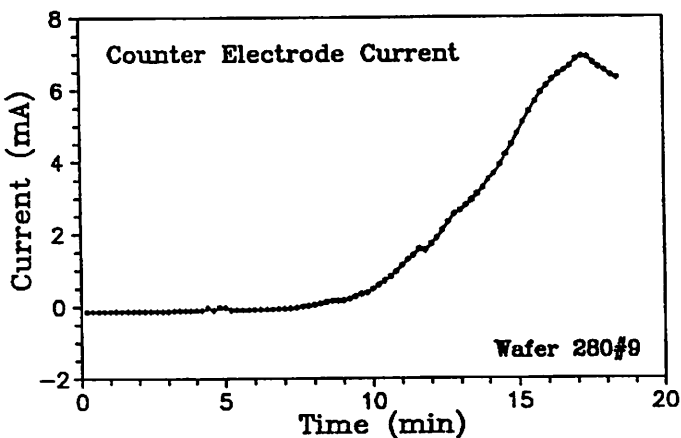


Fig. 4.4: Counter Electrode Current recorded during the last 20 minutes of the etching. The current peak, indicating passivation, is clearly visible.

This was due to its shallow depth (5µm) together with its relatively low surface concentration.

Leakage current flowing through the n-well caused a voltage drop and shifted the potential below the passivation point potential. When etching with a higher potential applied to the n-well, this problem could be overcome.

By displaying the Counter Electrode current I_{CE} , the termination of the etch process can easily be monitored. When the etching stops at the junction, the current first reaches a maximum and then decreases slowly. Figure 4.4, recorded during the etching of a device wafer, illustrates this behaviour. The current rise during the last 10 minutes of the etching is clearly visible. After the peak the wafer was kept for a short time in the solution.

The applied potentials in this particular case were $V_p = -1.5V$ and $V_n = 3V$ (With respect to the RE). With Infrared Spectroscopy we measured a diaphragm thickness of $8.3\mu m$, which was very constant over the whole wafer. Given a junction depth of $5\mu m$, the etching therefore stopped about $3\mu m$ before it. This outcome is in agreement with the results obtained by [30].

4.3. Simulated / measured parameters

Process simulations were carried out with the process simulator Suprem III. In Appendix C the input file is listed.

The $5\mu m$ deep n-well was implanted and driven-in for 8h at $1150^\circ C$. Spreading Resistance measurements on different test samples showed a depth of $4.8 \pm 0.2\mu m$. In the next figure both the simulated and measured concentration profiles can be seen. The first minimum indicates the junction depth of the p-implant (resistances), the second one the depth of the n-well.

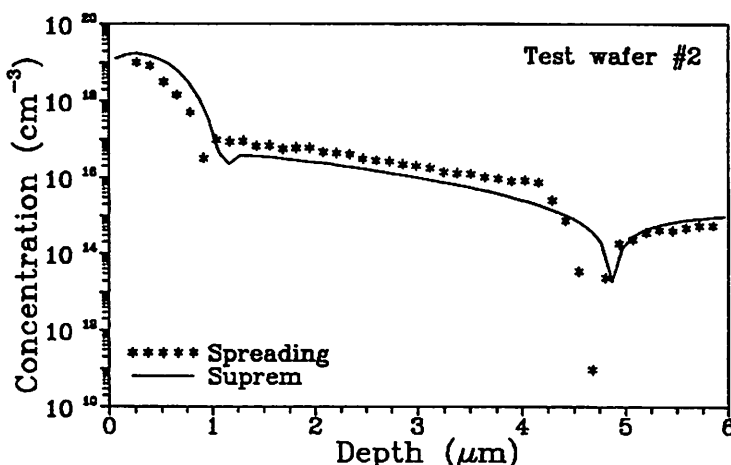


Fig. 4.5: Concentration profiles of a test wafer, simulated with Suprem and measured with Spreading Resistance.

For the final passivation layer a thermal oxide of 1500\AA thickness was chosen. We therefore

shortened the wet oxidation step of the 'standard' 2500Å thick thermal oxide based on the Suprem simulation result. Since this oxidation also activated the resistor implant impurities, a shorter oxidation time was desirable in order to keep the depth of the resistors shallow and their lateral diffusion small. The oxide obtained had a thickness of 1500Å, a favourable coincidence, since Suprem oxide growth predictions are normally in the range of $\pm 15\%$ of the obtained value.

In the next table, the simulated and measured sheet resistances of the resistors are summarized. Remember that values of 100 and 200 Ω/\square , respectively, were projected. These results are valid for both groups with passivation oxide and passivation oxide/nitride, since the nitride was deposited at 800°C and the deposition did not contribute to the thermal budget of the process.

Sheet resistance (Ω/\square)	Simulation Suprem III	Four Probe measurement
p-resistors: Passivation 1500Å SiO ₂	201 92	214 92
n-well	500-550 (depending upon substrate resistivity)	410

Table 4.1: Measured and simulated sheet resistances.

Measurements of membrane thicknesses of wafers etched with the same bias yielded the following results. The uniformity across the wafer was very high, this could be observed even with the naked eye.

Wafer 280#3:	8.3µm
Wafer 280#9:	8.3µm
Wafer 280#12:	8.2µm

The measurements, performed with infrared spectroscopy (FTIR), were carried out at the University of Barcelona.

4.4. Encapsulation / Anodic bonding

To facilitate the measurements, single resonator device chips were mounted on a standard 24-pin ceramic package and wire bonded. In the first attempt we glued single chips directly onto the package with an epoxy resin. However the hardening of the resin, performed in an oven at 200° C for 2 hours, induced large stresses in the chips. As a result, some of the initially straight bridges buckled, and others had resonance frequencies far above the expected values. A mounting leading to much lower stress levels was achieved by bonding the device wafers first onto a glass substrate before packaging. Common Pyrex from Dow Corning (#7740) was used.

4.4.1 Principle

Bonding of a silicon substrate onto a glass wafer, the so-called anodic or electrostatic bonding, is a well known process [39,40]. Encapsulation and packaging of sensors by anodic bonding are of great importance in the field of micromachining. Special glasses with thermal expansion coefficients equal to that of silicon over a wide temperature range, guarantee stress free assemblies. A widely used glass is Pyrex #7740 from Dow Corning. It is available in all standard wafer sizes (we used 1mm thick 4" Pyrex wafers) and it consists of 80% SiO_2 , 12% B_2O_3 , 3.7% Na_2O and 0.02% K_2O .

Anodic bonding is accomplished at temperatures between 200 and 450°C (below the melting point of aluminium). The silicon piece and the glass are brought into contact and a potential of 200-1000V is then applied, with the silicon as the anode. The electrostatic attraction between the glass and the silicon pieces pulls them into close contact, thus there is no need for applying mechanical pressure. Depending on the areas to be bonded, the process takes between a few minutes up to half an hour (e.g. for a 4" wafer).

A schematic bonding set-up is shown in Fig. 4.6.

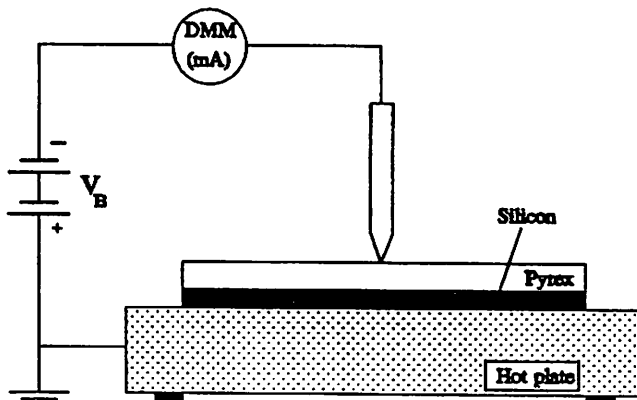


Fig. 4.6: A schematic setup for electrostatic bonding of silicon to glass.

The polished surface of the silicon is placed against the glass wafer or piece and the whole assembly

is heated on a chuck. A cathode electrode is brought into contact with the outer surface of the glass wafer. The electrical contact to the silicon anode is made either via the chuck or via an underlying aluminium piece.

At elevated temperatures, the positive sodium and potassium ions in the glass become mobile and they migrate towards the negative electrode on the glass surface. In the glass, permanently bound negative ions are left. They form a space charge layer between the glass-silicon surface, causing most of the applied potential to drop across this surface region. The extremely high electrical field in this region pulls the wafers into intimate contact. Moreover, negatively charged oxygen ions are transported out of the glass to bond with the silicon surface. Between the final glass-silicon bond, a very thin grown layer of SiO_2 can be observed [41].

Best bond results are obtained when bare silicon surfaces are bonded. However silicon wafers with thin layers of silicon oxide or silicon nitride have also been successfully bonded to glass [42]. Another possibility is the anodic bonding of silicon to silicon. In this method a thin glass film is sputtered onto one of the silicon wafers [43].

4.4.2 Bonding of the resonator devices

For bonding the first resonator device samples, we used a simple hot plate for heating. A metallized silicon wafer, serving as anodic contact to the silicon chip, was placed onto the heating plate. On this wafer we placed the device chip - glass chip sandwich. A high voltage source provided voltages up to 1200V. Monitoring the current during the bonding is a visual method to determine the end of the bond process. The current shows a peak when applying the voltage and then drops sharply. When the bond is completed, the current has decreased to negligible values. By bonding test chips we determined experimentally the best conditions for bonding the resonator devices wafers, which all had an oxide/nitride film on the wafer backside. At a temperature of 350°C and a potential of 1000V, applied for 30 minutes, the chips bonded successfully.

The latest chips could be bonded with a special equipment for wafer to glass/wafer to wafer bonding from Plasmos. The heating system in this machine consists of halogen lamps, mounted under the transparent quartz chuck, which can provide temperatures up to 550°C. Moreover the whole setup is located in a chamber which can be evacuated, thus bonding under various pressure conditions, including vacuum, is possible. We used the same conditions as above and obtained the same results. The bonded chips were finally glued onto a package and wire bonded.

V Measurements

Although the silicon bridges fabricated were designed for thermal excitation and piezoresistive detection, there are several driving and sensing possibilities to test their operation capabilities and their resonance characteristics.

Piezoelectric as well as electrostatic/capacitive operation must both be discarded. They require bridge structures with specific electrodes, different from the fabricated ones.

Three feasible schemes, taking into account the bridge structure consisting of a low doped silicon body with diffused resistors, exist. Apart from thermal excitation/piezoresistive detection, both photothermal excitation/optical detection and acoustical excitation/detection are possible. Depending on the available equipment, we performed two types of measurements. While in both cases the bridges were driven electrothermally, the motion was either detected with the piezoresistive resistors or measured optically. The measurements are described in detail in the next subsections. However we will briefly discuss the photothermal and acoustical drive principles.

Photothermal driving

This is based on thermal excitation with a light source [44]. Usually a laser diode, a He-Ne laser or a light emitting diode (LED) pulsed at the resonant frequency of the resonator is used. When focused onto the stress-sensitive part of the resonator, just like electrothermal heating, a periodic temperature gradient generates the necessary bending moment. Zhang et al. [45] presented silicon bridges that were driven by this method. By focusing a light beam onto the centre of a silicon bridge, they could excite its odd resonant modes, which are symmetrical around the bridge centre. For driving small structures, like our bridges, an optical system to focus the light beam and to concentrate the power incident on the resonator would be required. Another important aspect in photothermal driving is the surface material of the resonating element. A bare silicon surface is not suitable for efficient drive of thin structures, since optical frequencies can penetrate up to some tens of microns into the substrate and heat it. As a consequence the temperature gradient in the structure and thus the bending moment would be small. Therefore layers with a low optical absorption depth are normally deposited on top of the resonator to increase the photothermal conversion efficiency. Aluminium, especially, has a very low absorption depth of some tens of nanometres at optical frequencies [46]. Moreover its thermal expansion coefficient is about ten times higher than that of silicon, supporting the thermal drive mechanism.

Acoustical excitation/detection

Acoustical driving is based on excitation through sound-waves. The resonator is set into vibration by sound pressure. A basic setup consists of a loudspeaker, focused onto the resonator, emitting at its vibration frequency [47]. The reverse principle can be used for detection. A microphone, placed into close contact, registers the varying sound pressure of the vibrating resonator [48]. Since an

acoustically driven resonator cannot be sensed acoustically, acoustical excitation is mostly coupled with optical detection or vice versa.

5.1. Electrical measurements

5.1.1. Experimental Setup

The next Figure shows the experimental setup for electrical operation and detection. It is similar to the one proposed by Bouwstra [49]. A network analyzer (HP 4195A) was used to determine the transfer function of the resonator. For gain/phase measurements, the analyzer provides a sinusoidal output signal at the source channel (S). It is applied to a) the reference channel (R) and b) the input of the electrical circuit to be measured. The output of the circuit is connected to the test channel (T) of the analyzer. With this setup the transfer function between input and output of an electrical circuit can be measured. A resonator bridge can be considered as an electrical two-port with the excitation resistance corresponding to its input and the detection resistance corresponding to its output.

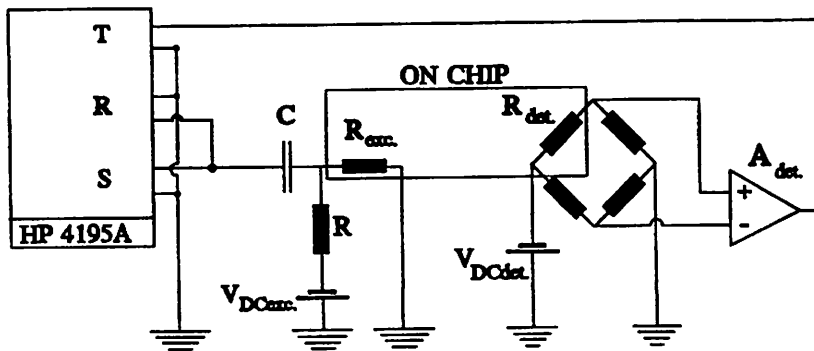


Fig. 5.1: Experimental setup for electrical operation.

For the measurements, the sinusoidal signal of the source channel of the analyzer was superimposed on a DC bias. This voltage was applied to the excitation resistance. Three heating components can be distinguished:

$$P_{exc} = \frac{1}{R_{exc}} \cdot [V_{DCexc} + V_{ACexc} \sin(\omega t)]^2 \quad (5.1)$$

$$= \frac{1}{R_{exc}} \cdot [V_{DCexc}^2 + 0.5 \cdot V_{ACexc}^2 + 2 \cdot V_{DCexc} \cdot V_{ACexc} \sin(\omega t) - 0.5 \cdot V_{ACexc}^2 \cos(2 \cdot \omega t)] \quad (5.2)$$

$$P_{exc} = P_{stat} + P_{dyn1} + P_{dyn2} \quad (5.3)$$

P_{dyn2} is irrelevant in the measurement, due to the frequency filtering by the analyzer. The DC component P_{stat} causes a static temperature elevation of the bridge, while the dynamic component P_{dyn1} causes a dynamic temperature elevation. This dynamic part sets the bridge into vibration. The vibration is detected by the piezoresistive detection resistance. The AC part of the output of the Wheatstone bridge is proportional to the vibration amplitude, to the Gauge factor of the resistance and to the supply voltage V_{DCdet} of the Wheatstone bridge. This part is buffered (A_{det}) and applied to the test channel of the analyzer.

The decoupling capacitor C together with the resistance R form a high pass filter. Their values ($R=100\Omega$, $C=470nF$) were chosen so that the 3dB frequency was far below the measurement frequency range used. A buffer A_{det} at the output of the Wheatstone bridge was necessary for two reasons. First the test channel had a low input resistance of 50Ω . Moreover one input of the test channel was internally grounded while both output nodes of the Wheatstone bridge were floating.

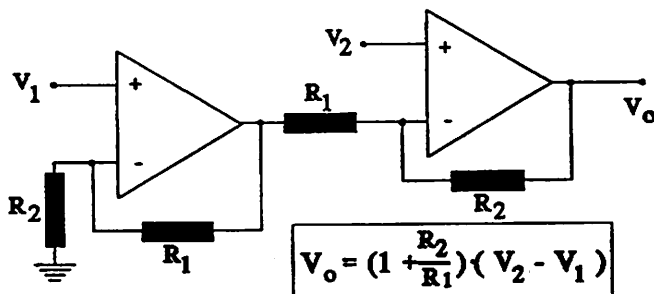


Fig. 5.2: Schematic of the Buffer A_{det} .

The chosen buffer circuit has the advantage of a very high input resistance. We tested different detection circuits, such as, for example, simpler buffers in combination with only a half bridge instead of a full bridge. However the best results were obtained with the setup shown.

Remark: Excitation could be simplified by taking a sinusoidal voltage and rectifying it. In this way a DC bias, which only contributes to undesired static heating, could be avoided. However the frequency spectrum of this waveform contains many harmonics with the result that the amplitude of the first harmonic is reduced. Tests revealed that bridges could also be driven with this, but the resonance peaks were less marked.

The transfer function which is measured is the sum of three transduction mechanisms. Mechanical transduction caused by the vibration of the bridge, electrical transduction on-chip, the so-called cross-talk, and transduction of the off-chip circuitry.

$$H(j\omega) = [H_{vibration}(j\omega) + H_{cross-talk}(j\omega)] * H_{circuitry}(j\omega) \quad (5.4)$$

$H_{circuitry}$ is the transfer function of the off-chip circuitry. Before making a measurement, $H_{circuitry}$ was determined for the same sweep range and then subtracted from the measured data. In this way the gain and phase shift introduced by the circuitry were eliminated.

$H_{cross-talk}$ represents the transfer function of undesired cross-talk. The cross-talk is the transduction effect of the bridge via the electrical domain. For example, metal pads and lines of the resistors represent substrate capacitances with the underlying oxide. Through these capacitances the two resistors are coupled capacitively. Moreover, the reverse biased diodes formed by the p-resistances and the n-well represent capacitances. In Figure 5.3 the capacitive paths between the two resistors on a bridge are schematically illustrated. An equivalent electrical circuit is derived in Figure 5.4. Note that the scheme is simplified, the components with little influence are omitted.

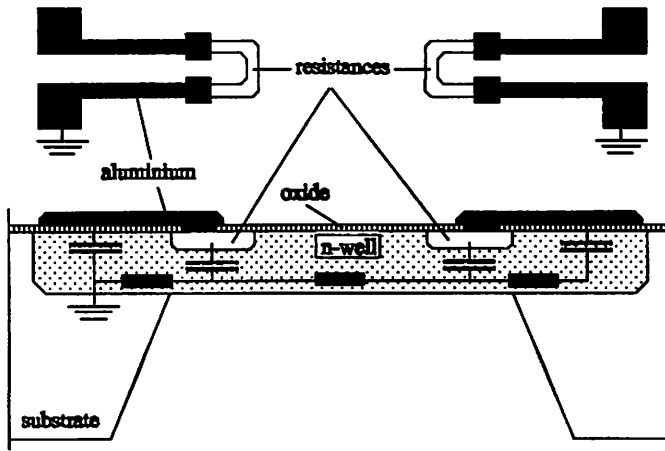


Fig. 5.3: Schematic of a resonator bridge showing the parasitic capacitances.

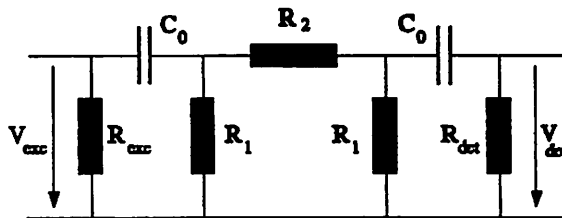


Fig. 5.4: Equivalent circuit of Figure 5.3.

Proceeding from the equivalent circuit, the transfer function between the two resistors can be calculated. For $\omega C_0 R_{det} \ll 1$, $\omega C_0 R_1 \ll 1$ and $\omega C_0 R_2 \ll 1$:

$$H_{cross-talk} = \frac{V_{ACdet}}{V_{ACexc}} \approx \frac{R_{det} R_2^2}{R_1} (\omega C_0)^2 \quad (5.5)$$

The cross-talk turns out to be 40dB/dec. Figures 5.5 and 5.6 show two transfer functions of a resonator bridge. For the plot in Figure 5.6 the excitation voltage contained both the DC and AC part, a resonance peak at a frequency of approximately 80kHz can be seen. For the plot in Figure 5.5 the DC excitation bias was turned off, thus only $H_{\text{cross-talk}}$ appears. An almost straight 40dB gradient can be observed in both graphs, confirming the above estimation.

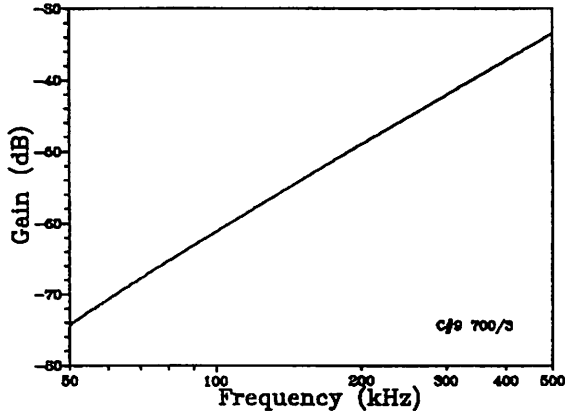


Fig. 5.5: Gain vs. frequency. $V_{\text{exc}}=V_{\text{AC}}$.

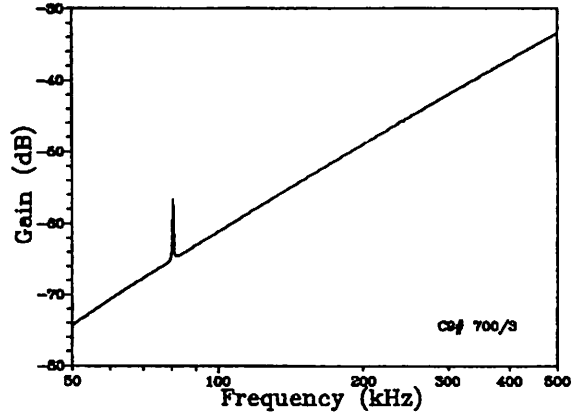


Fig. 5.6: Gain vs. frequency. $V_{\text{exc}}=V_{\text{DC}}+V_{\text{AC}}$.

5.1.2 Results

The transfer functions of the different bridges were determined for several combinations of DC and AC voltages for excitation in order to find a combination for which the transfer functions showed a peak. The supply voltage V_{DCdet} was kept constant at 5V. This value was found to be a good compromise between low thermal contribution of the detection resistor and an acceptable peak height. Resonance peaks could be detected on all of the 700 μm long bridges and on most of the 500 μm long ones. Peaks of the shorter bridges (300 and 400 μm) were either very small (peak height <1dB) or could not be localized. For that reasons, measurements were concentrated on the longer bridges.

Efficiency of excitation and detection

Figure 5.7 shows Bode plots of the transfer function of a 700 μm long single bridge for a frequency sweep from 65 to 85 kHz. Both excitation ($1.9\text{k}\Omega$) and detection resistors ($1.9\text{k}\Omega$) of this bridge were located at the ends. All measurements were made with $A_{\text{det}}=2$.

The peaks in $H(j\omega)$ represent the resonance frequencies of the same bridge. They were recorded by changing the static driving power V_{DCexc} . As can be seen, with increasing driving power the resonant frequencies shift to lower values. Increasing driving power involves an increase in temperature of the bridge and thus expansion and higher compressive stress. The left peak, situated at a frequency of 72.6kHz and with a height of approximately 13dB, was obtained with a total driving power of 34.2mW. On the other hand, when exciting with a total power of 9mW, resonance occurs at 82.6kHz. Note that when doubling the DC driving bias the incident driving power is quadrupled.

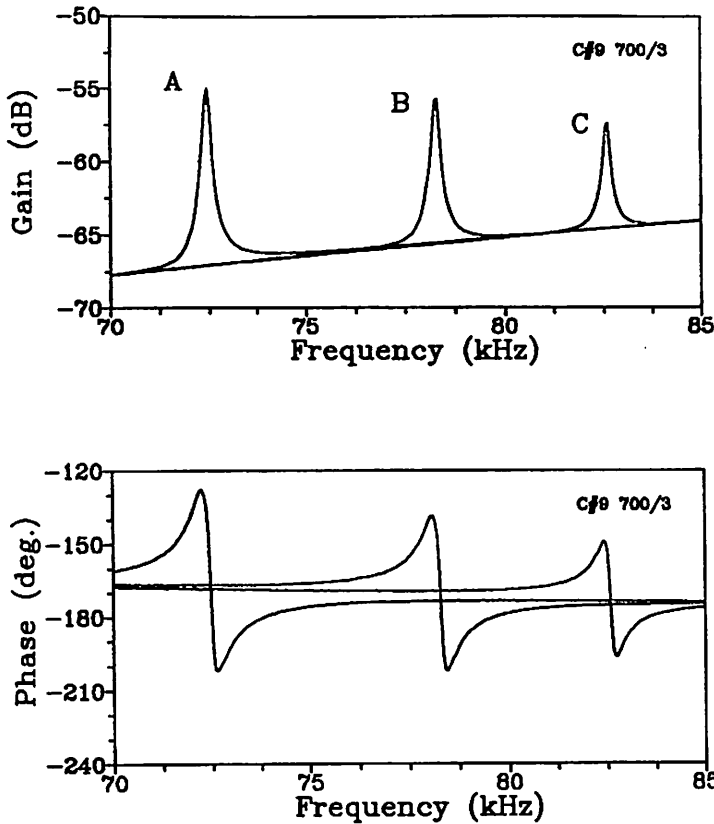


Fig. 5.7: Bode plots of a $700\mu\text{m}$ long bridge. $V_{AC_{exc}}=1\text{V}$;
 (A) $V_{DC_{exc}}=8\text{V}$ $P=34.2\text{mW}$; (B) $V_{DC_{exc}}=6\text{V}$ $P=19.5\text{mW}$; (C) $V_{DC_{exc}}=4\text{V}$ $P=9\text{mW}$.

The widths of the peaks reveal a quality factor of about 200. This value was confirmed by the optical measurements.

As a matter of fact the phase lag around resonance is not evident at first sight. From section two we would expect a total phase shift of 180° and a phase lag of 90° at resonance. The present phase plots however exhibit a phase maximum followed by a minimum, and the total phase shift is approximately zero.

This unexpected phase behaviour as well as the non-symmetric gain curves, in the above plot it is difficult to see because of the small frequency range, are attributed to the cross-talk between the two resistors. In Appendix D we give a qualitative explanation of this effect.

The thickness of this particular bridge was measured as $5.7\mu\text{m}$ (FTIR), giving a theoretical resonance frequency of 90.1kHz . The lower measured frequencies are due to the compressive stress, induced by the power dissipation due to the heating.

Similar results for efficiency of excitation and detection were obtained for resonator bridges with other resistor pattern. For $500\mu\text{m}$ long bridges the peaks were less marked. We obtained peak heights of 0.5 to 3dB. However it is remarkable that peaks could be detected at all, at the measurement frequency range of between 150 and 200kHz.

Resonance of triple bridges

As mentioned in section 3.2, the gain/phase plot of a triple bridge should exhibit three resonance peaks in close proximity, corresponding to the different oscillation modes. In mode one, all bridges oscillate in phase. In mode three, the outer ones oscillate with a phase of 180° with respect to the central bridge. Finally in mode two, which is in frequency very close to mode three, only the outer bridges resonate, with a phase difference of 180° .

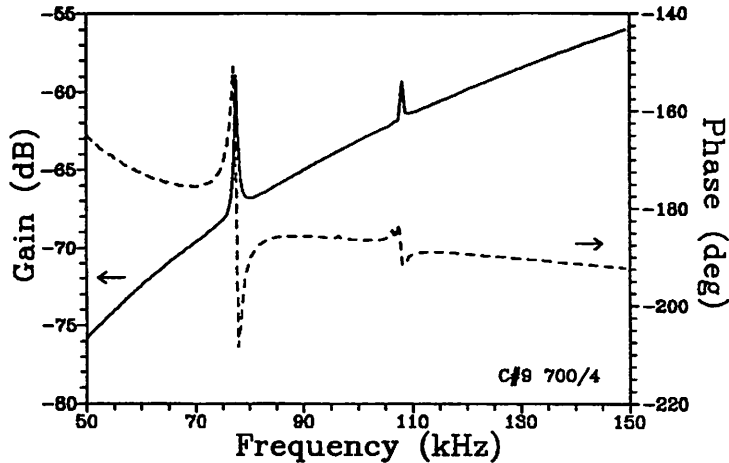


Fig. 5.8: Bode plot of a $700\mu\text{m}$ long triple bridge.

$$V_{ACexc}=1\text{V}, V_{DCexc}=5\text{V}; P=13.7\text{mW}.$$

Figure 5.8 shows the transfer function of a $700\mu\text{m}$ long triple bridge. Two peaks, indicating resonance in mode one and three respectively, could be detected. It is obvious that the peak corresponding to mode two is not visible, since in this mode the central bridge, where the two resistors are located, is at rest. For that reason both excitation and sensing of this mode are impossible.

Although the peak at the lower frequency is higher, the quality factor of this common mode oscillation is lower than that of the differential mode. Optical measurements revealed quality factors of 170 for the common mode and 380 for the differential mode for this particular bridge. The bridge thickness is $5.16\mu\text{m}$ (FTIR), corresponding to a theoretical resonance frequency of 81.6kHz in common mode oscillation. This value agrees well with the measured resonance frequency of 77.4kHz .

Reproducibility of bridge geometry and resonance frequency

To show whether bridge dimensions and thus resonance frequencies are reproducible across a wafer and from wafer to wafer, a 'mapping' of two wafers with the same bridge thicknesses was carried out. The resonance frequencies of identical bridges of 10 chips were measured.

Kloeck [38] reports that when using a four-electrode etch-stop technique the membrane thickness can be controlled to within $\pm 0.2\mu\text{m}$ standard deviation. This value corresponds to a standard deviation of

2.4% (of the mean thickness t) for our bridges. Given that the thickness is directly proportional to the resonance frequency f_R , the measured standard deviations of f_R are all within this range.

Bridge length (in μm) / bridge type	Wafer280#9		Wafer280#3	
	\bar{f}_R (in KHz)	s.d. (in % of \bar{f}_R)	\bar{f}_R (in kHz)	s.d. (in % of \bar{f}_R)
700/A	147.3	1.4	141.5	1.3
700/B	137.4	2.05	133.6	1.5
700/C	136.2	1.9	137.1	1.7
500/A	272.3	1.65	264.8	2.8
500/B	256.6	2.5	262.9	1.3
500/D	257.6	2.4	263.5	1.6

Table 5.1: Measured mean resonance frequencies and calculated standard deviations of identical bridges of a sample of 10 chips.

It can thus be concluded that with the four electrode etch stop technique the bridge thickness and so the resonance frequencies of silicon bridges can be controlled to within a range of a few percent. With the results obtained, the resonance frequency f_R of $700\mu\text{m}$ long and $6\mu\text{m}$ thick bridges would be controllable to within a range of better than $\pm 3\%$.

Influence of resistor position and driving power on the resonance frequency

For comparing the effect of the position of excitation and detection resistors and of the influence of the driving power, the resonance frequencies of bridges with different resistor positions were measured. We chose one bridge with three resistances, two at the ends and one in the centre. Additionally, another bridge with both resistances at the ends was used. All contact pads of the latter one were located on the same side, like type B in Figure 5.9. Both bridges were $700\mu\text{m}$ long and had a thickness of $6.3\mu\text{m}$. In Figure 5.10 their measured resonant frequencies versus the applied drive power are plotted, with variation in the DC excitation bias.

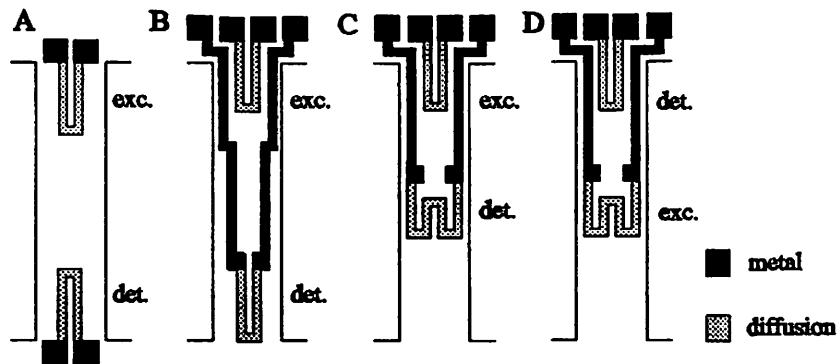


Fig. 5.9: Different positions of excitation and detection resistors.

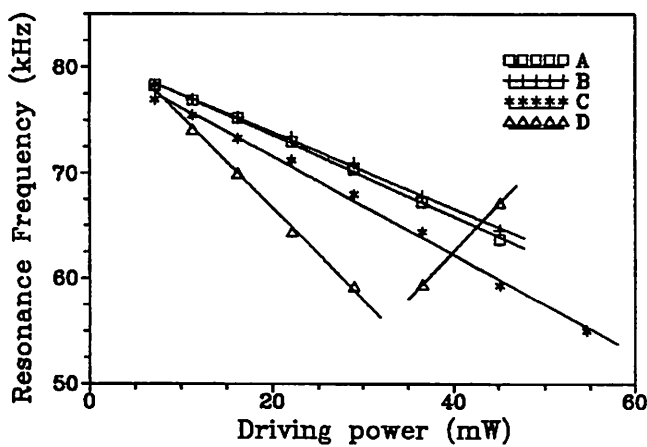


Fig. 5.10: Resonance frequencies versus input power of above bridge designs. $V_{ACexc}=1V$, V_{DCexc} varying.

It can be observed that the resonant frequency of the bridge with the excitation resistance in the centre, is most susceptible to variations in the driving power. Above a driving power of approximately 30mW, the bridge starts buckling and from this point the resonant frequency increases with further increasing driving power [50]. For bridge types A and B the measured frequency shift versus driving power is $0.5\text{Hz}/\mu\text{W}$ ($\alpha_r=6\cdot10^{-4}\ \mu\text{W}^{-1}$). A static power input of $1\mu\text{W}$ corresponds, for the given bridge resistance, to a DC drive bias of 45mV.

Influence of passivation film(s) on the resonance frequency

As expected, the residual stress of the passivation film(s) on the bridge has an important influence on f_R . The differences between measured and expected resonant frequencies of bridges with different passivation film(s) are listed in Table 5.2.

The effect on f_R of both the compressive oxide and the tensile nitride passivation is evident. It shows that even thin passivation layers can induce large residual stresses in the bridges. From this point of view the ideal solution would be a bare silicon bridge without any passivation film. However a

passivation film is required to isolate and protect the diffused resistors. Either a very thin grown oxide film of a few 100Å's, or a deposited oxide film are proposed for future applications.

Passivation layer (in Å)	Bridge length/thickness (in μm)	Difference $f_{R,\text{meas.}} - f_{R,\text{theor.}}$ (in %)
1800Å Si ₃ N ₄ + 1500Å SiO ₂	700/8.3	+15.7
	500/8.3	+11.8
1500 SiO ₂	700/6.4	-5.8
	500/6.5	-4.7

Table 5.2: Difference of measured and theoretical f_R of bridges with different passivation films.

5.2. Optical measurements

5.2.1. Experimental Setup

Optical measurements refers, in our case, to optical readout of the oscillation, where excitation of the resonator is electrothermal. Before discussing the experimental setup used for the measurements, we will explain the working principle of a vibrometer.

Working principle of a laser vibrometer

Vibrometers are usually utilized for surface vibration analysis. One of their advantages is that the measurement is performed without any mechanical contact with the object. A coherent laser beam is focused onto the moving object. Part of the incident light is reflected at its surface. Through the movement of the object the frequency of the reflected light is Doppler-shifted. The frequency shift is analyzed in a signal processor and converted into an output signal.

A laser-vibrometer is based on the principle of a Mach-Zehnder-interferometer, as represented schematically in Figure 5.11 [51,52]. Light from a laser is split up into two beams (Beam splitter BS1), the reference beam (1) and the measurement beam (2). The reference beam is reflected from the beam splitter BS3 and arrives directly the detector.

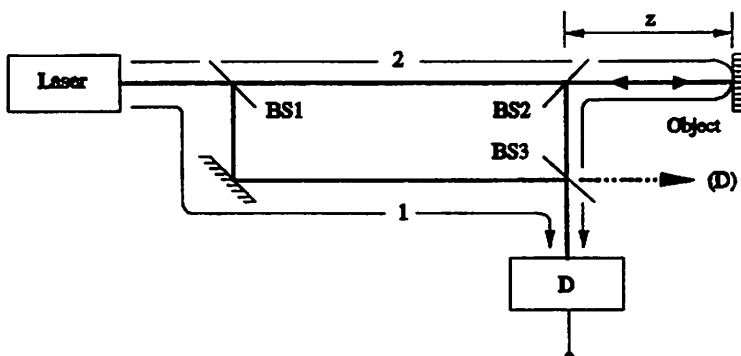


Fig. 5.11: Schematic representation of a Laser-Doppler-Vibrometer.

The measurement beam reaches the detector after being partially reflected from the object to be measured and from BS2. In BS3 the interference signal of the two beams is generated and then detected by the detector. All the information about position and speed of the object is contained in this interference signal. A second reference beam, indicated with dashed lines in Figure 5.11, can be detected by a second detector and processed. This technique reduces the noise-level of the detection system.

For deriving mathematically the Doppler shift, we consider the light emitted by the laser as an electromagnetic field $E_0(t)$. The field of the reference beam after having passed BS3 can then be

described as

$$E_1 = E_1(t) = \frac{1}{2} E_0(t - \tau_i) \quad (5.8)$$

where τ_i is the time the light needs to travel from the laser to BS3 and the factor 0.5 results from the beam splitting in BS1 and BS3. We derive E_2 in the same manner, considering the additional time needed to arrive at the object and to be reflected

$$E_2 = E_2(t) = \frac{1}{2} E_0(t - \tau_i - \tau_o) \quad (5.9)$$

τ_o is related to z , the distance to the object to be measured

$$\tau_o = \frac{2z}{c} \quad (5.10)$$

where c is the velocity of light in the medium between BS2 and object. Assuming a monochromatic light source with $E_0 = A \exp(-i\omega t)$, equations (5.8) and (5.9) can be written as

$$E_1 = \frac{1}{2} A e^{-i\omega t} e^{i\omega \tau_i} \quad (5.11)$$

$$E_2 = \frac{1}{2} A e^{-i\omega t} e^{i\omega(\tau_i + \tau_o)} \quad (5.12)$$

The intensity of an electromagnetic field is generally expressed as $I \sim |E_1 + E_2|^2$ [52]. In our case we obtain from equations (5.11) and (5.12) the intensity arriving at the detector (E_1^* are the conjugate complex values of E_1)

$$\begin{aligned} I &\sim (E_1 + E_2)(E_1^* + E_2^*) \\ &= |E_1|^2 + |E_2|^2 + 2 \operatorname{Re}(E_1 E_2^*) \\ &= \frac{I_0}{2} (1 + \cos \Delta\phi) \end{aligned} \quad (5.13)$$

where I_0 is the intensity emitted by the light source and $\Delta\phi$ the phase shift between measurement and reference beam

$$\Delta\phi = 4\pi \frac{z}{\lambda} \quad (5.14)$$

λ is the wavelength of the laser light. Equations (5.13) and (5.14) show that the intensity changes

periodically if the distance z increases. The period is one half of the wavelength. If z changes linearly with time, meaning that the object is moving with a constant velocity v , the detector receives a periodic signal with the frequency

$$f = f_D = \frac{2v}{\lambda} \quad (5.15)$$

This frequency is the well known Doppler frequency. The signal we derive for a constant velocity of the object is the following:

$$I = I_0 [1 + \cos(2\pi f_D t)] \quad (5.16)$$

It can easily be seen that because of the characteristics of the cosine function in equation (5.16), the sign of the velocity of the moving object and thus its movement direction, cannot be recognized.

By shifting the frequency of E_1 with respect to E_2 , this problem can be overcome. In this case ω in equation (5.11) has to be substituted by

$$\omega \rightarrow \omega + \omega_B \quad \omega_B = 2\pi f_B \quad (5.17)$$

where ω_B , f_B represent the frequency shift. We obtain instead of equation (5.16):

$$I = I_0 (1 + \cos[2\pi(f_B + f_D)t]) \quad (5.18)$$

When measuring a static object, a signal with frequency f_B is observed at the detector. This frequency shifts to higher or lower frequencies when the object is moving, depending upon the sign of v . In this way the direction of the movement can be recognized. In Figure 5.12 the practical realization of a frequency modulation in a vibrometer is shown.

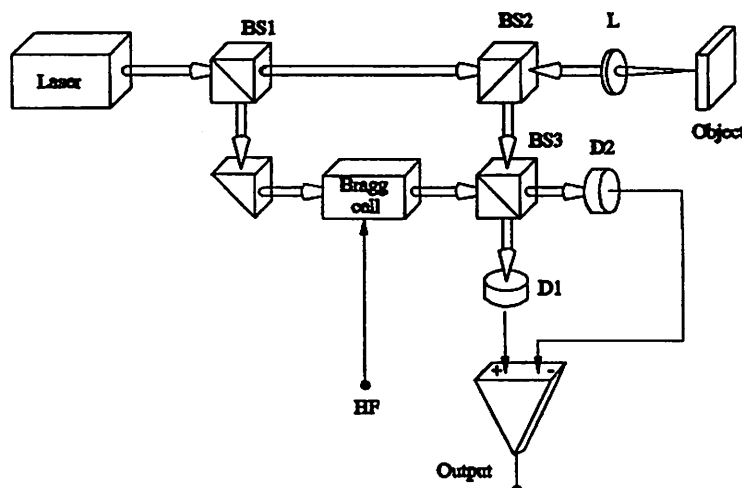


Fig. 5.12: Schematic structure of a laser-vibrometer with frequency modulation of the reference beam.

The reference beam is frequency-modulated with a Bragg cell. A common modulation frequency for

vibrometers is 40Mhz.

The vibrometer we used, (Polytec OFV-1102-HR), is equipped with a He-Ne laser light source (average power < 1mW). A minimum spot width of $50\mu\text{m}$ allowed precise focusing onto the bridge surfaces, whose widths were about in the same size. The velocity measurement range extends from 0 to $20.000\text{mm}\cdot\text{s}^{-1}$ with a bandwidth of 0.5MHz. Velocity or amplitude could be measured. Due to the limited bandwidth of 50kHz for amplitude measurements, the measurements made were suspect, and the data produced was therefore not evaluated.

Instead we divided the measured velocity values by the angular frequency ω , assuming that the velocity signal was harmonic.

Setup

In the next figure the complete experimental setup for optical readout can be seen. A Spectrum Analyzer (HP 3588A) provides a sinusoidal signal, that is superimposed on a DC bias and applied to the excitation resistor of the silicon bridge.

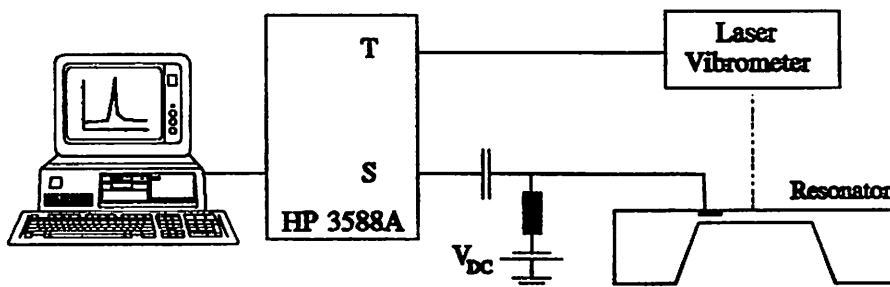


Fig. 5.13: Experimental setup for optical readout.

The laser beam is focused onto the bridge centre. A camera monitors the exact beam position. Moreover a display on the vibrometer, that indicates the intensity of the reflected beam at the detector, serves for accurate focusing. The analog output of the vibrometer is connected to the test channel of the analyzer. Via an IEEE interface, the analyzer is controlled by a PC and the spectrum obtained can be transformed directly into a velocity/amplitude spectrum.

5.2.2. Results

The excitation voltage V_{ACexc} was provided by the spectrum analyzer and V_{DCexc} by an external voltage source, as shown in Figure 5.13. As in the electrical measurements, the resistance and capacitor values were 100Ω and 470nF respectively. Since during the electrical measurements $V_{ACexc}=1\text{V}$ and a bias of $V_{DCexc}=5\text{V}$ for excitation was found to result in adequate peak heights, we used these voltages throughout all optical measurements. The laser beam spot was focused onto the centre of the bridge, where amplitude and velocity have a maximum. The incident power of the laser on the bridge was about 0.8mW , several times lower than in the experiments with piezoresistive detection (a typical

heating power of the detection resistor was in the range of some mW).

In Figure 5.14 the velocity spectrum of a 700 μm long bridge around its first resonance frequency is shown. The velocity was measured in the centre of the bridge and the values are maximum values. That means they indicate the velocity when the bridge passes through the zero deflection point. Resonance occurs at a frequency of 73.6kHz. The frequency we found when using piezoresistive detection was 71.2kHz. The higher value of the resonance frequency for optical readout is due to the lower thermal impact of the laser beam.

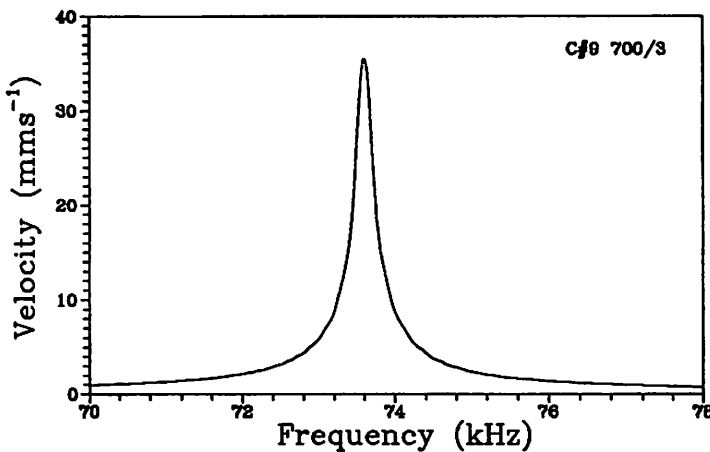


Fig. 5.14: Velocity spectrum of a 700 μm long bridge.

From the width of the peak, we obtain a Q value of 220 for this particular bridge. This value is typical for 700 μm long bridges, the devices we measured all had Q factors around 200.

At resonance, the maximum measured velocity of the bridge centre is 35.4 mm s^{-1} . This velocity is achieved when the bridge centre passes through the zero deflection point. From subsection 1.2 we know that the amplitude of a clamped-clamped beam oscillating at its first vibration mode has a sinusoidal shape, as written in equation 5.19.

The velocity at $x=x_0$ can be obtained by simply deriving equation 5.19

$$A(t, x=x_0) = A_{0,x_0} \sin(2\pi ft) \quad (5.19)$$

$$v(t, x=x_0) = 2\pi f A_{0,x_0} \cos(2\pi ft) \quad (5.20)$$

For the given velocity we thus find the amplitude spectrum by dividing the velocity values with the angular frequency. Doing so, a resonance amplitude of 0.08 μm at the bridge centre results. This value is typical, for other bridges with the same length we found amplitudes in the order of about 0.08...0.09 μm .

In Figure 5.15 a spectrum of the same bridge over a larger frequency range can be seen. For comparing the peak heights, the velocity is represented on a logarithmic scale. The first and the

second harmonic have an approximately 10 times smaller amplitude and velocity. The three resonance frequencies occur at $f_{M1}=73.3\text{kHz}$ (84.6kHz), $f_{M2}=233.8\text{kHz}$ (233kHz) and $f_{M3}=480.7\text{kHz}$ (457.2kHz).

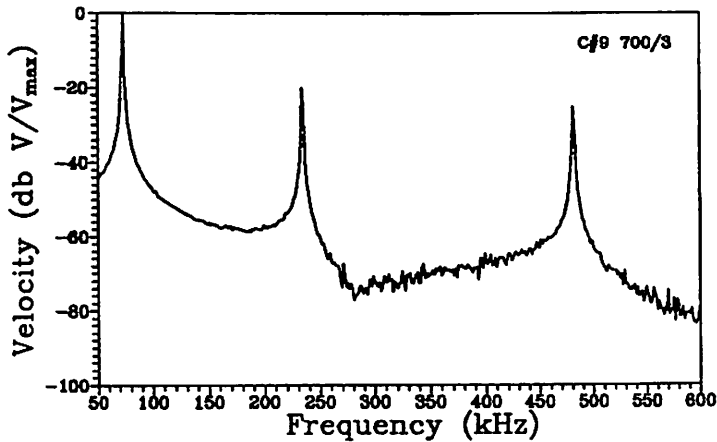


Fig. 5.15: Velocity spectrum of a 700μm long bridge.

In Figure 5.16 a velocity spectrum of a 700μm long triple bridge is shown. The three different first vibration modes can clearly be seen. As expected, the differential mode oscillation (corresponding to the right peak) has a higher Q-factor than the common mode oscillation.

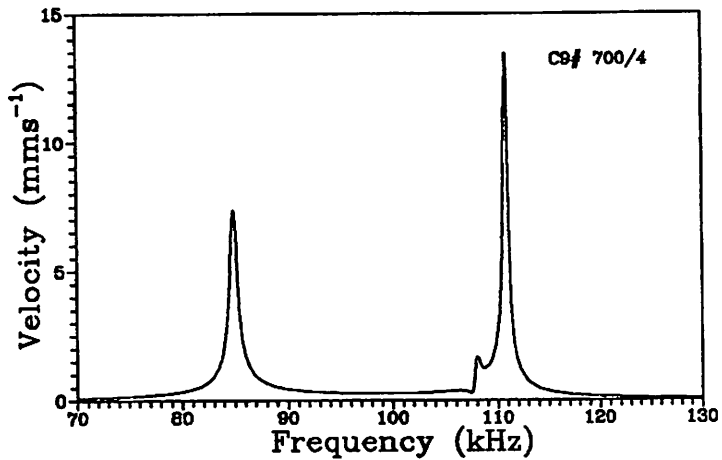


Fig. 5.16: Velocity spectrum of a 700μm long triple bridge.

From the graph we obtain $Q_D \approx 380$ for the differential mode (right peak) against $Q_C = 170$ for the common mode (left peak 5.1). When calculating the maximum velocity at resonance again using equation 5.20, it turns out that the value does not coincide with that found for single bridges. The maximum velocities of triple bridges are somewhat smaller than those of single bridges. One probable explanation is that when focusing the laser beam onto the bridges, it could have covered partially the central bridge and one or both of the lateral bridges. This is very possible, since the bridges of the triple bridge are all narrower than the beam spot. In this way, in the differential mode, a velocity signal consisting of two signals with a phase angle of 180° would have been measured, the

superposition of this signals resulting in a smaller measured velocity than the effective one.

Figure 5.17 shows a spectrum over a larger frequency range of the same bridge. The harmonics up to a frequency of 700kHz (!) of the three different first modes are visible. The velocity is also shown on a logarithmic scale.

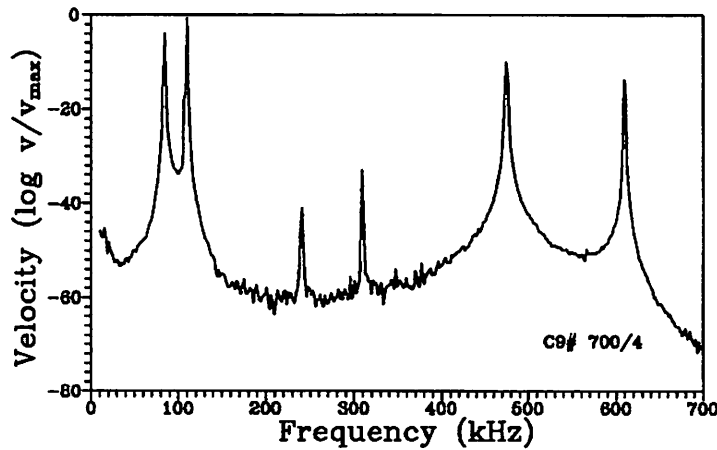


Fig. 5.17: Velocity spectrum of a 700 μm long triple bridge.

Finally we present two velocity spectra of 500 μm long bridges. We would expect that resonance amplitudes diminish at higher frequencies, since it is not likely that the maximum velocity of a bridge increases drastically for smaller bridge length. Indeed the measured velocities are similar to those of the 700 μm long bridges, therefore the amplitudes are smaller.

The following resonance frequencies were calculated analytically, and measured:

Chip:	Thickn. (FTIR)	$f_{\text{theor.}}$	$f_{\text{meas.}}$
Single bridge C#11 500/2	6.1 μm	214.7kHz	213.2kHz
Triple bridge C#11 500/6	5.6 μm	197.1kHz	191.8kHz

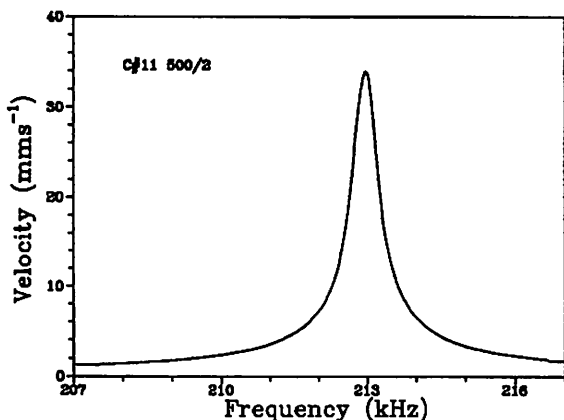


Fig. 5.18: Velocity spectrum of a 500 μm long single bridge.

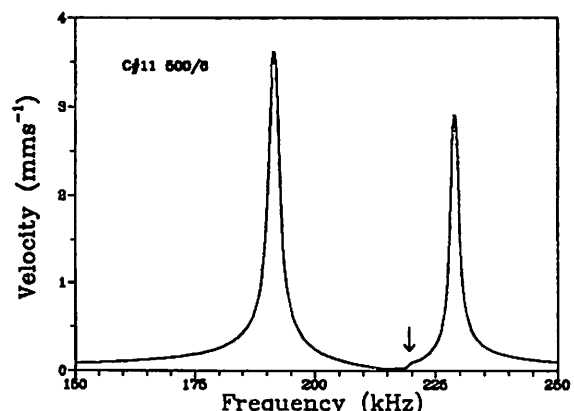


Fig. 5.19: Velocity spectrum of a 500 μm long triple bridge.

From the peak velocity we calculate a maximum amplitude of 25nm of C#11 500/2 at resonance. The quality factors we obtain are $Q=550$ for the single bridge and $Q_C=200$ and $Q_D=600$ for the triple bridge. In Figure 5.19 a small "ramp" at approximately 219kHz, marked by an arrow, indicates the second basic oscillation mode of the triple bridge.

In total we measured 10 different encapsulated bridges. The results are consistent. Q values range from about 200 for 700 μm long bridges to about 500 for 500 μm long bridges. As the spectra for triple bridges show, all three basic resonance modes could be excited and detected, in contrast to the electrical measurements. However the difference between the common and differential resonance mode is not as large as expected, we found a factor 2..3 for Q_D/Q_C .

The measured velocity spectra are maybe not as evident as amplitude spectras, but by assuming a sinusoidal oscillation we could calculate the maximum amplitudes from the peak velocities. They are in the order of 0.1 μm for 700 μm long bridges, whereas those for 500 μm long bridges are smaller by a factor 4.

When finally comparing the resonance frequencies obtained by optical measurements with those of the electrical measurements, it is seen that the first method gave higher frequencies, due to the smaller thermal impact of the light beam, but the absolute difference is minor and the results agree well.

f_{rea} (in kHz)	Analytical value	Optical measurement	Electrical measurement
<u>Single bridges:</u>			
C#9 700/3	79.4	73.6	67.3
C#9 700/5	91.1	89.86	84.1
C#10 7002	-	87.4	80.9
C#10 700/5	92.1	90.1	84.3
C#11 500/2	214.7	213.2	210.2
<u>Triple bridges:</u>			
C#9 700/4	86.4 / -	84.9 / 110.8	77.4 / 108.1
C#10 700/4	91.1 / -	96.8 / 122	86.9 / 117.9
C#11 500/6	197.1 / -	197.75 / 229	194.7 / -

Table 3: Comparison between optical and electrical measurements

For both types of measurements we chose identical excitation voltages, in this way the data is comparable.

VI Conclusions

The present report describes the design, fabrication and characterization of silicon resonator bridges. The initial aim of the project, testing the feasibility of the thermal drive principle applied to micromachined silicon bridges, has been entirely achieved. We demonstrate that thermally excited and piezoresistive driven microbridges can be used in a future acceleration sensor as a resonant element. This sensor is being developed as a continuation of this work and will be fabricated soon - the results presented here influenced both the sensor design and the projected process.

The bridge structures consist of a low doped silicon body with two implanted piezoresistive resistors and a thin passivation layer on top. One resistor serves for electrothermal excitation and the other one for piezoresistive detection of the bending mode vibration of the bridge.

For the fabrication of the devices, we used an electrochemical etch-stop technique, previously developed at CNM, for precise definition of the thickness of membranes obtained by anisotropic wet etching. A separate dry etch process for etching silicon up to a depth of 15 µm was developed. Final stress-free mounting for the characterization was achieved by bonding resonator chips anodically to rigid glass chips. This bonding process was not studied extensively, just enough to determine the parameters needed for a satisfactory bond.

The complete fabrication process of the resonator bridges, (and of a set of piezoresistive accelerometers designed in the same maskset and fabricated at the same time), can be employed as a basic micromachining process for the fabrication of a multitude of sensor structures, e.g. for measuring force, pressure and acceleration.

Results of the measurements

Marked resonance peaks (peak height 10..15dB) could be excited and measured electrically up to frequencies of 100kHz. At higher frequencies the peak height decreases drastically, for 500µm long bridges resonating at approximately 200kHz we obtained peak heights in the order of 1.3dB. Therefore a minimum bridge length of about 600µm together with a thickness of 5..6µm are recommended for future applications.

The resonance peaks of single bridges (length 700µm) had quality factors in the range of 200, in air. This value was confirmed from both electrical and optical measurements. For triple bridges, a difference of factor 2..3 in the quality factors of the basic differential and common resonance mode were obtained. In numbers, a typical Q value of the differential mode of a 700µm long triple bridge is 400. For the application in a resonant accelerometer that has to meet high resolution standards, a triple bridge with a high Q-factor, and thus a higher frequency definition, is clearly preferred.

Reproducibility of bridge dimensions, and thus resonance frequencies, are directly related to the electrochemical etch-stop, which allows a membrane thickness control to within $\pm 0.2\mu\text{m}$ standard deviation. With the results we obtained, the resonance frequency of a $700\mu\text{m}$ long and $6\mu\text{m}$ thick bridge is therefore controllable to within a range of better than $\pm 3\%$.

The ideal resistor positions with respect to driving and sensing efficiency, as well as temperature sensitivity, were found to be at the ends of the bridge.

According to the optical measurements, a typical maximum velocity of a $700\mu\text{m}$ long resonating bridge is 35.2mm/sec. , measured at the bridge centre. From this velocity we deduce an amplitude at resonance of about $0.09\mu\text{m}$, also at the bridge centre. More impressive than these numbers is the fact that resonance peaks of thermally driven bridges could be measured up to a frequency of 700kHz ! The clear, noise-free spectra of the optical measurements permitted, moreover, an exact determination of the Q-factor of the devices.

As expected, the passivation layer on the $5\mu\text{m}$ thick silicon bridges plays an important role. Both thin silicon nitride and oxide films shifted the basic resonance frequencies, indicating a non-negligible residual stress. With respect to this, but even more to the temperature dependent stress of 'sandwiched' layers, passivation film(s) on the bridge should be avoided completely or, if not possible, kept as thin as possible. A recommendation is either a very thin thermal oxide in the range of some 100\AA or a deposited oxide.

As the bridges were driven with an AC voltage superimposed on a DC bias, the latter induces undesired static heating. We measured, for a specific bridge design with a $1.9\text{K}\Omega$ heating resistor, a temperature sensitivity of $0.5\text{Hz}/\mu\text{W}$ ($\alpha_t=6\cdot10^5 \mu\text{W}^{-1}$). A static driving power of $1\mu\text{W}$ corresponds to a DC drive bias of 45mV .

One drawback of the resonator concept as presented is the capacitive coupling of the implanted resistors, that is inherent and cannot be eliminated completely. Thus part of the electrically measured transfer functions must be attributed to the so-called cross-talk, signal transfer between the resistors via capacitive paths. This effect means that the typical phase shift of 180°C , although present, cannot be observed directly in the Bode plots. However when switching to a Re/Im representation of the transfer function, the typical resonance circle is present. Our model, taking into consideration the cross-talk, justifies the experimental results and explains the formation of the transfer function that is a superposition of mechanical resonance and electrical cross-talk.

Despite the cross-talk the resonance peak of the fundamental vibration mode could be detected in practically all of the tested samples.

The cross-talk phenomena could be avoided by employing polysilicon resistors that are isolated by an underlying oxide. Doing this the fabrication process would only be slightly affected, however with polysilicon resistors, the underlying oxide and the silicon bridge body, a more temperature sensitive

structure would result. Still, for a future application the use of polysilicon ~~wires~~^{resistors} is not ruled out.

References

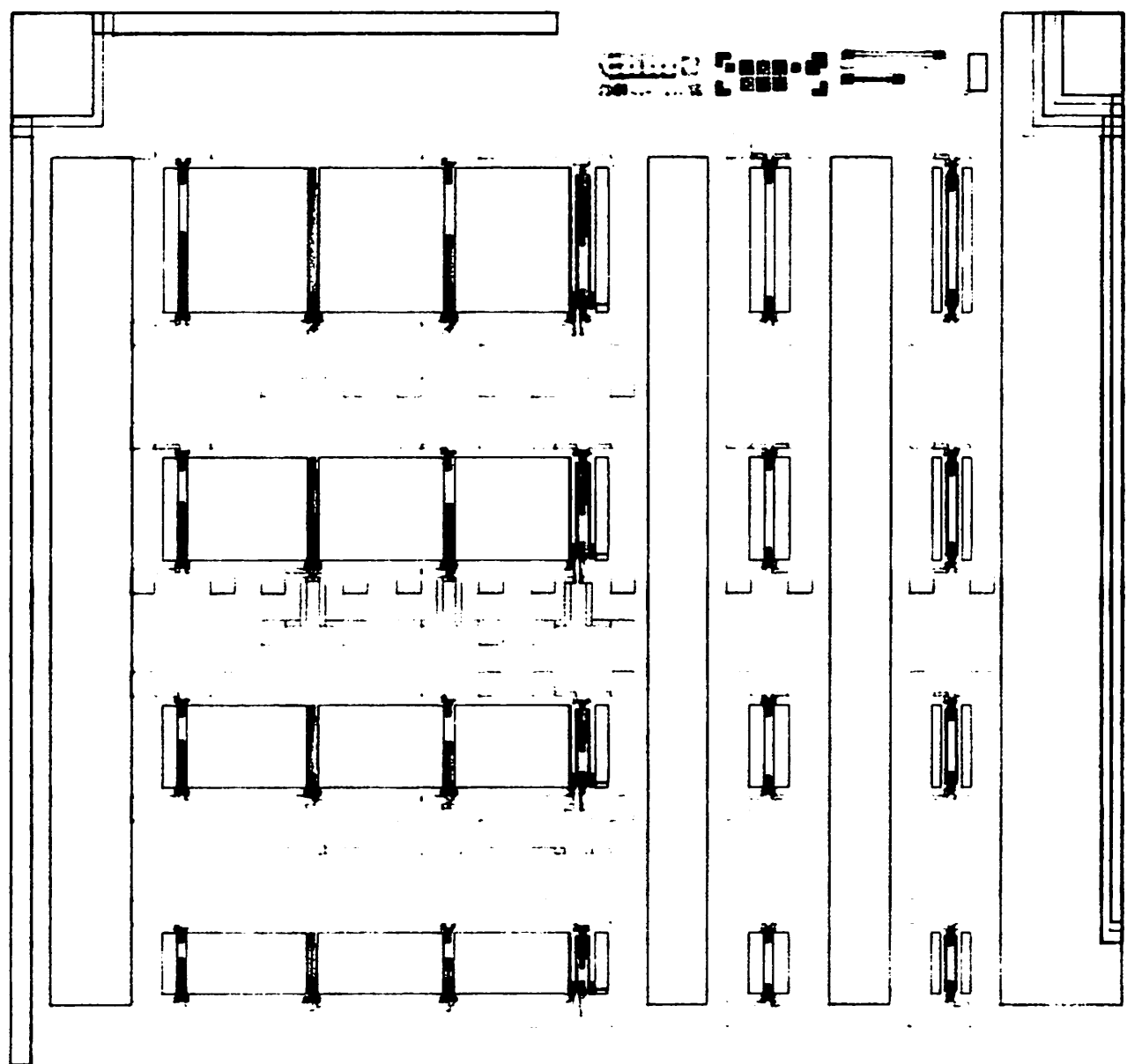
- [1] R.M. Langdon, Resonator sensors - a review, *J. Phys. E: Sci. Instrum.*, Vol. 18 (1985), pp. 103-115.
- [2] D. W. Satchell and J.C. Greenwood, A Thermally-Excited Silicon Accelerometer, *Sensors and Actuators*, 17 (1989), pp. 241-245.
- [3] S.C Chang, M.W. Putty, D.B. Hicks, C.H. Li and R.T. Howe, Resonant-bridge Two-axis Microaccelerometer, *Sensors and Actuators*; A21-A23 (1990), pp. 342-345.
- [4] K. Petersen, F. Pouramahdi, J. Brown, P. Parsons, M. Skinner and J. Tudor, Resonant Beam pressure Sensor Fabricated with Silicon Fusion Bonding, *Tech. Digest 6th. Int. Conf. Solid-State Sensors and Actuators (Transducers '91)*, San Francisco, CA, USA, June 24-28 (1991), pp. 664-667.
- [5] T.S. Lammerink, M. Elwenspoek, R.H. van Ouwerkerk, S. Bouwstra and J.H.J. Fluitman, Performance of Thermally excited Resonators, *Sensors and Actuators*, A21-A23 (1990), pp. 352-355.
- [6] T.S. Lammerink, M. Elwenspoek and J.H.J. Fluitman, Thermal Actuation of Clamped Silicon Microbeams, *Sensors and Materials*, 3,4 (1992), pp. 217-238.
- [7] R.J. Wilfinger, P.H. Barell, D.S. Chhabra, The Resistor: A Frequency Selective Device Utilizing the Mechanical Resonance of a Silicon Substrate, *IBM Journal Re. Developm.* 12, January 1968, pp. 113-118.
- [8] M.B. Othman, A. Brunnschweiler, Electrothermally Excited Silicon Beam Mechanical Resonators, *Electronics Letters*, Vol. 23, No. 14 (1987), pp. 728-730.
- [9] D. Moser, O. Brand and H. Baltes, A CMOS compatible thermally excited silicon oxide beam resonator with aluminium mirror, *Tech. Digest 6th. Int. Conf. Solid-State Sensors and Actuators (Transducers '91)*, San Francisco, CA, USA, June 24-28 (1991), pp. 547-550.
- [10] S. Bouwstra, R. Legtenberg, H.A.C. Tilmans and M. Elwenspoek, Resonating Microbridge Mass Flow Sensor, *Sensors and Actuators*, A21-A23 (1990), pp.332-335.
- [11] O. Brand, H. Baltes and U. Baldenweg, Thermally Excited Silicon Oxide Bridge Resonators in CMOS Technology, *MME'92, Third European Workshop on Micromachining, Micro-mechanics and Microsystems*, pp. 195-198.
- [12] V. Mosser, J. Suski, J. Goss and E. Obermeier, Piezoresistive pressure sensors based on polycrystalline silicon, *Sensors and Actuators A*, 28 (1991), pp. 113-132.
- [13] K.E. Petersen, Silicon as a mechanical material, *Proc. IEEE*, Vol. 70, May 1982, pp. 420-457.
- [14] H. Seidel, L.Csepregi, A. Heuberger, H. Baumgärtel, Anisotropic Etching of Crystalline Silicon in Alkaline Solutions, *J. Electrochem. Soc.*, Vol. 137, No. 11, Nov. 1990, pp. 3612-3626.

- [15] O. Tabata, R. Asahi, H. Funabashi and S. Sugiyama, Anisotropic etching of silicon in $(CH_3)_4NOH$ solutions, Tech. Digest 6th Int. Conf. Solid-State Sensors and Actuators (TRANSDUCERS'91), San Francisco, CA, USA, June 24-28 (1991), pp. 811-814.
- [16] W.R. Runyan and K.E. Bean, Semiconductor integrated circuit processing technology, Addison-Wesley Publishing Company, Inc., 1990.
- [17] H. Seidel, The Mechanism of Silicon Etching, Transducers '87, Rec. on the 4th Int. Conf. on Solid-State Sensors and Actuators 1987, pp. 120-125.
- [18] S.M. Sze, VLSI technology, McGraw-Hill, 1988.
- [19] E. Cabruja, M Schreiner, Deep Trenches in Silicon Using Photoresist as a Mask, to be published in Sensors and Actuators A.
- [20] C. Linder, T. Tschan and N.F. de Rooji, Deep Dry Etching of Silicon - A Novel Micromachining Tool, Sensors and Materials, Vol. 6, No. 6 (1992), pp. 311-324.
- [21] A.B. Pippard, The Physics of vibration, Cambridge University Press, Cambridge, GB (1990).
- [22] A. P French, Vibrations and waves, M.I.T Introductory physics series, G.B (1971).
- [23] C.M. Habermann, Vibration analysis, Charles E. Merill Publishing Comp., Columbus, Ohio (1988).
- [24] S.P. Timoshenko, D.H. Young and W. Weaver, Vibration Problems in Engineering, John Wiley & Sons, NY, 4th edn. (1974), Chapter 5.
- [25] H.A.C. Tilmans, M. Elwenspoek and J.H.J. Fluitman, Micro resonant force gauges, Sensors and Actuators A, 30 (1992), pp. 35-53.
- [26] R.D. Blevins, Formulas for natural frequency and mode shape, Robert E. Krieger Publishing & Co, Malabar, Florida (1984).
- [27] Prof. Bao, Notes on the lecture "Silicon Sensors", CNM (1992).
- [28] Y. Kanda, A graphical representation of the piezoresistive coefficient in silicon, IEEE Trans. Electron Devices ED-29 (1982), pp. 64-70.
- [29] Communication with Mr. Fabula from IMIT, Villingen-Schwenningen, Germany.
- [30] A Götz, S. Marco y J. Esteve, Paro Electroquímico en KOH, Nota técnica CNM 58/92, Julio 1992.
- [31] H.A. Waggener, Electrochemically controlled thinning of silicon, Bell System Technics Journal, Vol. 49, No. 3 (1970), pp. 473-475.
- [32] T.N. Jackson, M.A. Tischler and K.D.Wise, An Electrochemical P-N Junction Etch-Stop for the Formation of Silicon Microstructures, IEEE El. Dev. Letters, Vol. EDL-2, No.2, February 1981, pp. 44-45.
- [33] H. Norjiri and M. Uchiyama, Bias-dependent Etching of Silicon in aqueous Ammonia, Tech. Dig. 6th Int. Conf. on Solid-State S&A (Transducers '91), San Francisco, CA, USA (1991), pp. 136-139.

- [34] V.M. McNeill, S.S. Wang, K.Y. Ng and M.A. Schmidt, An Investigation of the Electrochemical Etching of (100) Silicon in CsOH and KOH, Tech. Digest Solid-State Sensor and Actuator Workshop, Hilton Head Island, South Carolina, June 4-7, USA (1990), pp. 92-97.
- [35] R.L. Smith, B. Kloeck, N.F. de Rooji and S.D. Collins, The potential dependence of silicon anisotropic etching in KOH at 60°C, J. Electrochem. Chem., 238 (1987), pp. 103-113.
- [36] O.J. Glembocki and R.E. Stahlbush, Bias-Dependent Etching of Silicon in Aqueous KOH, J. Electrochem. Soc., Vol. 132, No. 1 (1985), pp. 145-151.
- [37] H. Seidel, The mechanism of anisotropic, electrochemical silicon etching in alkaline solutions, Tech. Digest Solid-State Sensor and Actuator Workshop, Hilton Head Island, Soth Carolina, June 4-7, USA (1990), pp. 86-91.
- [38] B. Kloeck, S.D. Colins, N.F. de Rooji and R.L. Smith, Study of Electrochemical Etch-Stop for High-Precision Thickness Control of Silicon Membranes, IEEE Trans. On El. Dev., Vol. 36, No.4, April 1989, pp. 663-669.
- [39] Micromachining and Micropackaging of transducers, Elsevier Science Publishers B.V., Amsterdam, NL (1985), pp. 41-61.
- [40] K.B Albaugh, P.E. Cade, D.H Rasmussen, Mechanisms of Anodic Bonding of Silicon to Pyrex Glass, Techn. Digest of the IEEE Solid-State Sensor & Actuator Workshop, Hilton Head Island, South Carolina, USA (1988), pp. 109-110.
- [41] R. Stengl, T. Tan and U. Gösele, A model for the silicon wafer bonding process, Jpn. J. Appl. Phys., 28 (10) (1988), pp.1735-1741.
- [42] A. Hanneborg, M. Nese, H. Jakobsen, R. Holm, Silicon-to-thin film anodic bonding, Third Workshop on Micromachining, Micromechanics and Microsystems, June 1-2 (1992), Leuven, Belgium, pp. 9-19.
- [43] A. Hanneborg, N. Nese and P. Ohlckers, Silicon-to-silcicon anodic bonding, Tech. Digest, Micromechanics 1990, 2nd Workshop on Micromechanics, Berlin, 1990, pp. 100-108.
- [44] S. Venkatesh and B. Culshaw, Optically excited vibrations in micromachined silica structure, Electron. Lett., 21 (1985), pp. 315-317.
- [45] Zhang, D. Uttamchandani and B. Culshaw, Measurement of the mechanical properties of silicon microresonators, Sensors and Actuators A, 29 (1991), pp. 79-84.
- [46] D. Walsh and B. Culshaw, Optically Activated Silicon Microresonator Transducers: an Assessment of Material Properties, Sensors and Actuators A, 25-27 (1991), pp. 711-716.
- [47] L.M. Zhang, D. Walsh, D. Uttamchandani and B. Culshaw, Effect of optical power on the resonance frequency of optically powered silicon microresonators, Sensors and Actuators A, 29 (1991), pp. 73-78.

- [48] D. Moser, O. Brand and H. Baltes, A CMOS compatible thermally excited silicon oxide beam resonator with aluminium mirror, Tech. Digest 6th. Int. Conf. Solid-State Sensors and Actuators (TRANSDUCERS '91), San Francisco, CA, USA, June 24-28 (1991), pp. 547-550.
- [49] S. Bouwstra, R. Legtenberg, H.A.C. Tilmans and M. Elwenspoek, Resonating Microbridge Mass Flow Sensor, Sensors and Actuators A21-A23 (1991), pp. 332-335.
- [50] S. Bouwstra, Resonant Microbridge Mass Flow Sensor, Thesis, University of Twente, Enschede, The Netherlands (1990), Chapter 7.
- [51] A. Lewin, F. Mohr and H. Selbach, Heterodyn-Interferometer zur Vibrationsanalyse, Sonderdruck aus "Technisches Messen - tm" 57 (1990), Heft 9, pp. 335-345.
- [52] P. Hariharan, Optical Interferometry, Academic Press Australia, Marrickville, Australia (1985), Chapter 2.

Appendix A: Mask layout



Appendix B: Process listing

Wafer 1-4 are passivated with a 1500Å thick SiO₂ film. The dry etching mask is photoresist.
Wafer 5-8 are passivated with a 3200Å thick SiO₂ film. The dry etching mask is photoresist.
Wafer 9-12 are passivated with a 1500Å thick SiO₂ film plus a 1600Å thick Si₃N₄ film. The dry etching mask is LTO.

A batch of 12 wafers and 4 test wafers (T1-T4) was processed.

1	Mark wafers	1-12, T1-T4
2	Photolithography Mask CNM024 - L8 (for double-sided alignment)	1-12
3	Dry etch silicon (appr. 1500Å)	1-12
4	Remove Resist	1-12
5	Mark test wafers	T1-T4
6	Clean	1-12, T1-T4
7	Oxidation 2500Å	1-12
8	Photolithography Mask CNM024 - L2 (n-well implant), Insert ring	1-12
9	Etch oxide (2500Å)	1-12
10	Implant Phosphorus: $2 \cdot 10^{13} \text{ cm}^{-2}$ 150KeV	1-12, T1-T4
11	Strip Resist	1-12
12	Clean	1-12, T1-T4
13	Drive-in: 8h 1150°C (including oxidation) Measure oxide thickness!	1-12, T1-T4
14	Photolithography Mask CNM024 - L4 (p ⁺ -implant for contacts)	1-12
15	Etch oxide (appr. 7000Å)	1-12
16	Strip Resist	1-12
17	Implant Boron: $6 \cdot 10^{15} \text{ cm}^{-2}$ 50KeV Implant Boron: $7 \cdot 10^{15} \text{ cm}^{-2}$ 50KeV	1-4 y 9-12 5-8
18	Clean	1-12
19	Protection oxide (300Å)	1-12, T1-T4
20	Photolithography Mask CNM024 - L3 (p-implant for resistances) Test wafers: Cover 1/2 wafer	1-12, T1-T4
21	Etch oxide (appr. 7000Å, also areas with appr. 300Å)	1-12, T1-T4
22	Strip Resist	1-12, T1-T4
23	Implant Boron: $7 \cdot 10^{14} \text{ cm}^{-2}$ 50KeV (Sheet Res. appr. $200\Omega/\square$)	1, 2, 9, 10, T1

	Implant Boron: $2 \cdot 10^{15}$ cm ⁻² 50KeV (Sheet Res. appr. $100\Omega/\square$)	3, 4, 11, 12, T2
	Implant: Boron: $9 \cdot 10^{14}$ cm ⁻² 50KeV (Sheet Res. appr. $200\Omega/\square$)	5, 6, T3
	Implant Boron: $2.5 \cdot 10^{15}$ cm ⁻² 50KeV (Sheet Res. appr. $100\Omega/\square$)	7, 8, T4
24	Strip oxide	1-12, T1-T4
25	Clean	1-12, T1-T4
26	Oxidation (1500Å)	1-4 y 9-12, T1, T2
	Oxidation (4000Å). Measure oxide thickness, also test wafers	5-8, T3, T4
27	LPCVD Nitride (1600Å)	1-12
28	Photolithography Mask CNM024 - L6 (KOH etch patterning)	1-12
	Wafer backside, Insert ring	
29	Dry etch nitride (1600Å). Wafer backside	1-12
30	Dry etch nitride (1600Å). Wafer frontside	1-8
31	Strip Resist	1-12
32	Photolithography Mask CNM024 - L5 (Contact window openings)	1-12
33	Etch nitride (1600Å)	9-12
34	Etch oxide	1-12
35	Strip Resist	1-12
36	Clean	1-12
37	Metallization	1-12
38	Photolithography Mask CNM024 - L7 (Metallization)	1-12
39	Etch Metal	1-12
40	Strip Resist	1-12
41	Anneal Metal	1-12
42	Clean	1-12
43	Oxidation LTO (10.000Å)	9-12
44	Photolithography Mask CNM024 - L8 (Dry etch patterning)	1-12
45	Etch oxide (1µm LTO)	9-12
46	Dry etch nitride (1600Å)	9-12
47	Etch oxide	1-12
48	Strip Resist	9-12
49	Wet etching KOH	1-12
50	Clean	1-12
51	Dry etching silicon	1-12
52	Strip oxide	9-12
53	Strip Resist	1-8

Appendix C: SUPREM III Input file

```
INITIALIZE      SILICON <100> RESISTIV BORON=12 DX=.1 THICKNESS=15
PRINT          LAYERS ENABLE ELECTRICAL
COMMENT        n-well implant
IMPLANT       PHOSPHOR DOSE=2.5E13 ENERGY=150
COMMENT        annealing
DIFFUSION     TEMP=800 TIME=30 T.FINAL=1150 INERT
DIFFUSION     TEMP=60  TIME=1150 WETO2
DIFFUSION     TEMP=420 TIME=1150 INERT
DIFFUSION     TEMP=1150 TIME=30 T.FINAL=800
ETCH          OXIDE ALL
COMMENT        p+-contacts, 4000Å oxide
COMMENT       IMPLANT BORON DOSE=7E15 ENERGY=50
COMMENT        p+-contacts, 1500Å oxide
COMMENT       IMPLANT BORON DOSE=6E15 ENERGY=50
COMMENT        thin oxide 300Å
DIFFUSION     TIME=40 TEMP=800 T.FINAL=1000 F.N2=6
DIFFUSION     TIME=27 TEMP=1000 F.O2=6
DIFFUSION     TIME=40 TEMP=1000 T.FINAL=800 F.N2=6
COMMENT        ETCH OXIDE ALL
COMMENT        p-resistor implant, 200Ohm, 1500Å oxide
COMMENT       BORON DOSE=7E14 ENERGY=50
COMMENT        p-resistor implant, 100Ohm, 1500Å oxide
IMPLANT       BORON DOSE=2E15 ENERGY=50
COMMENT        p-resistor implant, 200Ohm, 4000Å oxide
COMMENT       BORON DOSE=9E14 ENERGY=50
COMMENT        p-resistor implant, 100Ohm, 4000Å oxide
COMMENT       BORON DOSE=2.5E15 ENERGY=50
COMMENT        activation
DIFFUSION     TEMP=8000 TIME=20 T.FINAL=950 F.N2=6
DIFFUSION     TIME=10 TEMP=950 F.O2=6
COMMENT        activation+ oxidation 1500Å
DIFFUSION     TIME=54 TEMP=950 F.O2=3.5 F.H2=5
COMMENT        activation + oxidation 4000Å
COMMENT       DIFFUSION TIME=129 TEMP=950 F.O2=3.5 F.H2=5
COMMENT       DIFFUSION TIME=10 TEMP=950 F.O2=6
DIFFUSION     TEMP=950 TIME=20 T.FINAL=800 F.N2=6 PRINT
ETCH          OXIDE ALL
PRINT          ELECTRICAL BORON PHOSPHORUS CONCENT
PLOT          CHEMICAL NET BOTTOM=1E13 TOP=5E20 DEVICE=REGIS
PLOT          CHEMICAL NET BOTTOM=1E13 TOP=5E20 DEVICE=HP7550
+  Timestam TIME.SIZ=0.3 X.SIZE=0.4 Y.SIZE=0.4 PLOT.OUT=N5.PLG
+  TITLE="Sum n-well with p-resistor"
```

Appendix D: Cross-talk and its influence on the phase lag

As derived in section 2, the gain of a mechanical harmonic oscillator has a maximum at resonance, accompanied by a total phase shift of 180° between excitation and response of the system. When representing the response of the system as a vector, its length expressing the gain and its angle with the positive x-axis the phase, a typical resonance circle results:

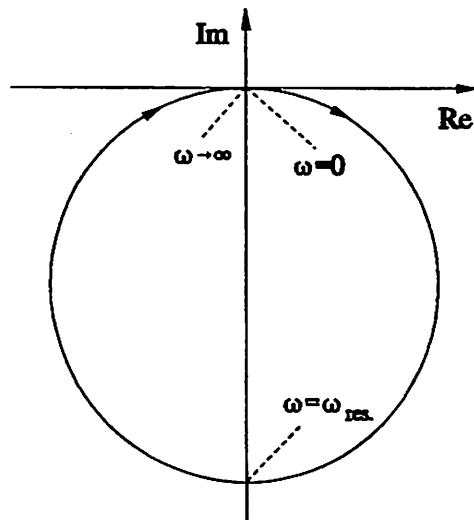


Fig. D.1: Resonance curve of a mechanical harmonic oscillator.

The circle is located in the third and fourth quadrant and passed through clockwise, according to the behaviour of the physical system.

The cross-talk of a resonator bridge can be described in the above representation as a vector that shifts the frequency origin of the circle. For simplicity let us assume a constant cross-talk (with respect to the frequency) with a slightly negative angle. The resulting resonance circle for this example looks then as drawn in Figure D.2.

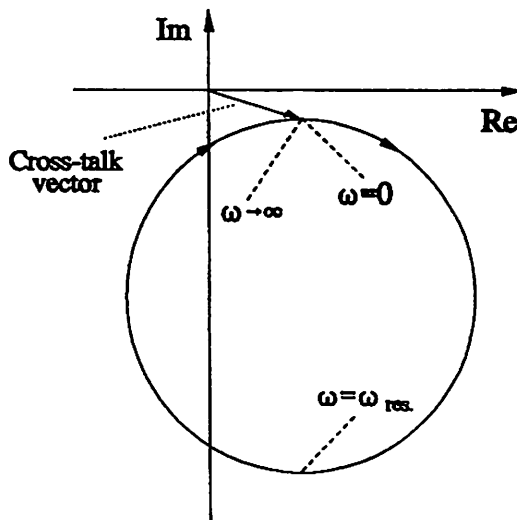


Fig. D.2: Resonance circle of an oscillator with constant cross-talk.

The transfer signal is a vectorial addition of the mechanical vibration and the electrical cross-talk, as illustrated in Figure D.3.

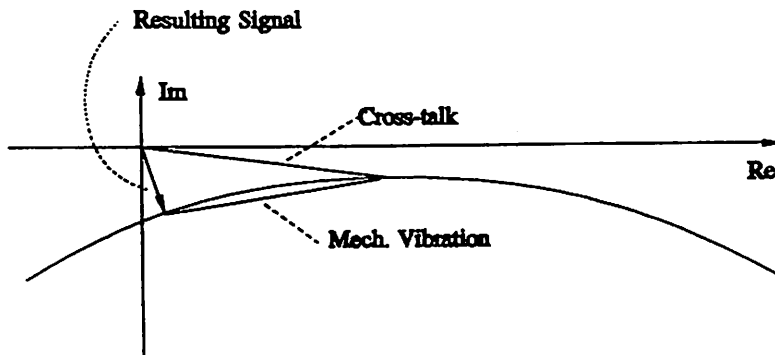


Fig. D.3: Vectorial addition of mechanical resonance and cross-talk.

Gain and phase lag at resonance have changed now. A gain maximum is observed just below resonance and a gain minimum just above resonance. In the same way the phase lag can be found, it has a maximum after passing through resonance, and the total phase shift is 0.

Depending on the length and angle of the cross-talk, the resonance circle can be situated in any of the four quadrants and a multitude of gain-phase shapes is possible.

In Figure D.4 a typical transfer function of a resonator bridge is shown. The phase lag for low frequencies is approximately 180° and it has a maximum below resonance and a minimum above.

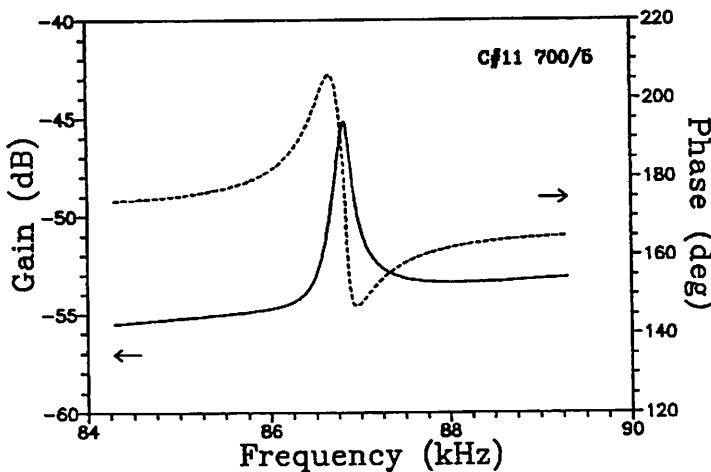


Fig. D.4: Transfer function of a resonator bridge.

The same function in a Real/Imaginary part representation leads to the known resonance circle in Figure D.6. Several effects are observed. Firstly, the cross-talk vector causes a phase shift of the whole circle of approximately 180° , resulting in a displacement along the real axis towards negative values. Second the circle is not closed, indicating that the cross-talk signal is not constant with respect to the frequency. Moreover the actual circle is turned by -90° .

In section five we derived a electrical circuit modelling the cross-talk, this is repeated in Figure D.5. It can be considered as a high-pass filter (C_0-R_1), followed by a voltage divider (R_2-R_1). This voltage divider

follows a second high-pass filter (C_0 - R_{det}). We found that the values of the parasitic capacitors are in the Picofarad range. Therefore the two high pass filters are driven far below their cut-off frequency, causing the 180° phase shift of the cross-talk vector and thus of the resonance circle.

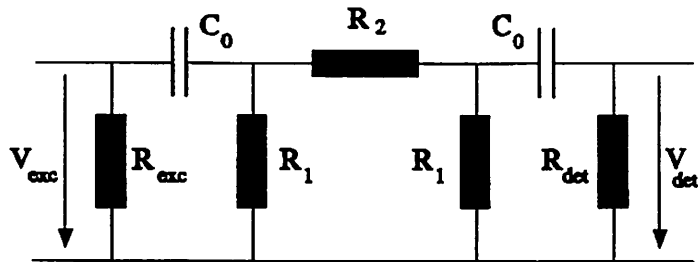


Fig. D.5: Equivalent circuit representing the cross-talk (see section 5.5.1).

The gain of the circuit in Figure D.5 is 40dB/dec., obtained by adding the gain of the two high-pass filters. This implies that the cross-talk vector increases for increasing frequencies, at the same time its phase lag decreases from 180° for small frequencies down to 0° for frequencies above the 3dB frequency of the filters.

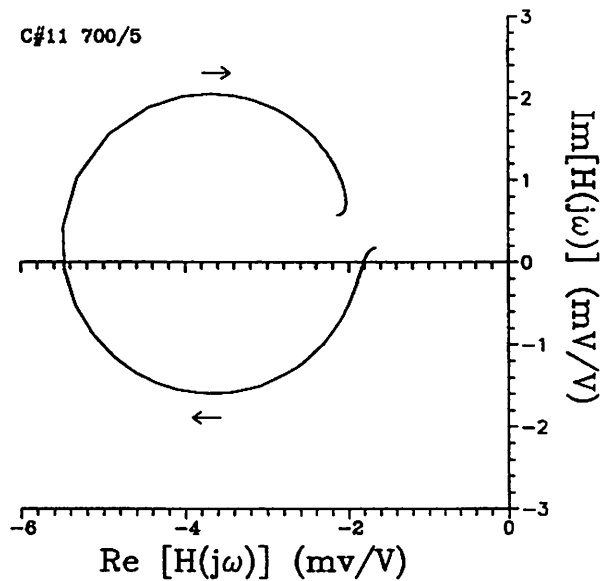


Fig. D.6: Resonance circle of a resonator bridge.

In the resonance circle in Figure D.6 this effect can be clearly seen. The end of the circle is further away from the origin and forms a smaller angle with the positive x-axis than at its beginning. If we had recorded a circle with a larger frequency span, the effect would be even more clearly visible.

All the bridges that we measured with the two resistances at the ends, showed the same gain/phase characteristics, indicating that the resonance circles are all situated in the second and third quadrant like the one in Figure D.6. For bridges that were driven or detected with a central resistor, the circles are still in the same quadrants, but turned by 180° . This is because the stress profile in the centre is the inverse of that at the end.